Spatially distributing monthly reference evapotranspiration and pan evaporation considering topographic influences

Tim R. McVicar [a,*], Thomas G. Van Niel [b], LingTao Li [a], Michael F. Hutchinson [c], XingMin Mu [d], ZhiHong Liu [d]

[a] CSIRO Land and Water and eWater Cooperative Research Centre, GPO Box 1666, Canberra, 2601 ACT, Australia
[b] CSIRO Land and Water and eWater Cooperative Research Centre, Private Bag No. 5, Wembley, 6913 WA, Australia
[c] Centre for Resource and Environmental Studies, The Australian National University, Canberra, 0200 ACT, Australia
[d] Institute of Soil and Water Conservation, Chinese Academy of Sciences, 26 Xinong Road, Yangling 712100, Shaanxi Province, China

Summary Many hydrological models engage spatially distributed measures of 'potential evapotranspiration' (ET_{pot}). The reliability and utility of the physically based Penman–Monteith approach to generate ET_{pot} has been recently advocated. Assuming land-surface conditions, spatial surfaces of reference evapotranspiration (ET_0) can be generated taking into account the topographic influence of forcing meteorological variables. This was performed in this paper by spatially interpolating maximum (T_{max}) and minimum (T_{min}) air temperatures, wind speed (u) and vapor pressure (e_a), using a spline model with a linear sub-model dependency on elevation, and modelling the radiation environment, taking topography (i.e., elevation, slope and aspect) into account, prior to calculating ET_0 at each grid-cell. In accordance with previous research, resultant lapse rates showed a strong seasonal pattern; values were steeper in summer than winter and those for T_{max} were steeper than for T_{min}. Monthly mean T_{max} lapse rates varied from $-3.01\,^\circ\text{C}\,\text{km}^{-1}$ in winter to $-7.69\,^\circ\text{C}\,\text{km}^{-1}$ in summer, with T_{min} lapse rates ranging from $-2.79\,^\circ\text{C}\,\text{km}^{-1}$ in winter, to $-6.64\,^\circ\text{C}\,\text{km}^{-1}$ in summer. Monthly climatologies of the near-surface elevation-dependence (NSED) for u and e_a also showed strong seasonal values. NSED of u varied from $2.01\,\text{ms}^{-1}\,\text{km}^{-1}$ in winter reducing to $0.75\,\text{ms}^{-1}\,\text{km}^{-1}$ in summer. The NSED for e_a ranged from $-0.08\,\text{kPa}\,\text{km}^{-1}$ in winter to $-0.64\,\text{kPa}\,\text{km}^{-1}$ in summer. For a 252-month sequence from 1980 through 2000, spatial surfaces of ET_0 with a 100 m resolution for the 113,000 km² study site located in the Loess Plateau, China were generated using an

* Corresponding author. Tel.: +61 2 6246 5741; fax: +61 2 6246 5800.
  E-mail address: Tim.McVicar@csiro.au (T.R. McVicar).

'interpolate-then-calculate' approach. Resultant ET_0 values varied from about 20 mm month^{-1} in winter to over 150 mm month^{-1} in summer. In order to assess the reliability of these ET_0 surfaces, pan evaporation (E_{pan}) was also spatially interpolated and from these a set of pan coefficient (K_{pan} — a unitless ratio defined as ET_0/E_{pan}) surfaces were calculated. Spatio-temporally averaged K_{pan} values for the study site varied from 0.44 in April to 0.65 in late summer. K_{pan} values were in agreement with another study using a Chinese 20 cm diameter micro-pan, and, as expected, were lower than other values documented using a Class A pan. The influence of topography, especially aspect, was seen on the resultant ET_0 and K_{pan}, but not E_{pan}, surfaces. Sensitivity analysis showed that results were particularly stable in the hydrologically active portion of the year extending from March to October, inclusive. This study demonstrated that high spatial resolution monthly surfaces of ET_0 can be spatially modelled while taking into account the influence of topography on the forcing variables.

Introduction

Many hydrological, agricultural and environmental models, including assessments of global water cycle intensification due to climate change (Huntington, 2006) and frameworks to predict impact of re-vegetation activities on regional hydrology (e.g., Donohue et al., 2007; McVicar et al., in press; Zhang et al., 2001), require a spatially distributed measure of 'potential evapotranspiration' (ET_{pot}). The generally accepted broad 'definition' of ET_{pot} is that it defines an upper limit of evapotranspiration if the land-surface for a given environment (meaning both meteorological and land-surface conditions Lhomme, 1997) was brought to saturation (Granger, 1989); noting that ET_{pot} is an idealised value as no feedbacks between the evaporating land-surface and the governing meteorological variables are included (Lhomme, 1997). That is, if a regional surface were evaporating at its potential the fact that this would alter atmospheric conditions, therefore changing rates of ET_{pot}, is not considered. For ET_{pot} to be a useful index, it must be calculated from readily available data (Lhomme, 1997), and it must be physically robust taking into account the known interactions between variables controlling evaporation (e.g., McKenney and Rosenberg, 1993; Monteith, 1965; Penman, 1948; Penman, 1956). For example, interactions between minimum air temperature, dew point and the corresponding vapor pressure deficit should be accounted for, especially when considering a changing climate.

Since the 1950s the concept of ET_{pot} has been increasingly used by more disciplines, for different purposes, and for vastly different climates, with the number of empirical definitions growing (e.g., Allen et al., 1998; Oudin et al., 2005; Xu and Singh, 2002 and the references therein); many of these were only calibrated locally. To encourage the use of a standard ET_{pot} the concept of 'crop reference evapotranspiration' (ET_0) was developed, which was calculated using four approaches in the mid 1970s (Doorenbos and Pruitt, 1975; Doorenbos and Pruitt, 1977). Following extensive analysis of the four methods in many locations world-wide, the Penman–Monteith approach (Monteith, 1965) was unanimously accepted (Smith et al., 1991) as the sole Food and Agricultural Organisation (FAO) endorsed approach to estimate ET_0, culminating in publication of Allen et al.'s (1998) FAO-56 report.

Development of ET_0 from the Penman–Monteith equation requires simplifying assumptions via the detailed definition of reference land-surface conditions. The Allen et al. FAO-56 report (1998, pp. 23) defines the land-surface conditions as: 'A hypothetical reference crop with an assumed crop height of 0.12 m, a fixed surface resistance of 70 s m^{-1} and an albedo of 0.23. The reference surface closely resembles an extensive surface of green grass of uniform height, actively growing, completely shading the ground and with adequate water. The requirements that the grass surface should be extensive and uniform result from the assumption that all fluxes are one-dimensional upwards'. Using these reference land-surface conditions, and given a few other assumptions, the FAO-56 formulation of ET_0 (Allen et al., 1998) is:

$$ET_0 = \frac{0.408\Delta(\boldsymbol{R_n} - \boldsymbol{G}) + \gamma\frac{900}{T+273}u_2(e_s - e_a)}{\Delta + \gamma(1 + 0.34u_2)} \tag{1}$$

where ET_0 is the reference evapotranspiration (mm day^{-1}); Δ is the slope of the saturation vapor pressure curve (kPa °C^{-1}); $\boldsymbol{R_n}$ is the allwave net radiation at the surface (MJ m^{-2} day^{-1}); $\boldsymbol{G}$ is the allwave ground heat flux (MJ m^{-2} day^{-1}); γ is the psychrometric constant (kPa °C^{-1}); T is the mean daily air temperature, that is $T = (T_{max} + T_{min})/2$ (°C), where T_{max} and T_{min} respectively are the daily maximum and minimum air temperatures (°C); u_2 is the daily average wind speed at 2 m above ground level (m s^{-1}); $e_s - e_a$ is the saturation vapor pressure deficit (kPa); with e_s being the saturation vapor pressure (kPa) and e_a the actual atmospheric water vapor pressure (kPa). Starting from the one-dimensional single-source formulation of the Penman–Monteith equation (Monteith, 1965) the FAO-56 ET_0 is fully derived, including explicitly expanding the 'few other assumptions', in several sources (e.g., Allen et al., 1998; McVicar et al., 2005a). If the time-step of all data are monthly then the resultant ET_0 is provided with units of mm month^{-1} (Allen et al., 1998; McVicar et al., 2005a).

To our knowledge there is only one previous case where ET_0 has been spatially distributed (Xu et al., 2006). This was performed for the entire Yangtze River basin with an approximate 25 km resolution output. Even though there is an elevation range of 6621 m, changes in meteorological conditions as a function of topography (e.g., Barry, 1992;

Dodd, 1965; Geiger, 1950; Raupach and Finnigan, 1997; Yoshino, 1975, among many others) were not incorporated in Xu et al.'s (2006) spatial modelling, which they performed using a 'calculate-then-interpolate' approach (McVicar and Jupp, 2002; Stein et al., 1991). By calculating ET_0 then spatially interpolating it geometrically in two dimensions (*i.e.*, longitude and latitude) means that topographic changes of key meteorological variables between the meteorological stations are not captured in their implementation (Xu et al., 2006). In another study, Chuanyan et al. (2004) spatially distributed the Hargreaves and Samni (1985) form of ET_{pot} (which is forced using only air temperature) and in contrast to the findings of Xu et al. (2006) they showed the importance of topography on the resulting ET_{pot} surfaces. However, the results from Chuanyan et al. (2004) study are not physically based as the reliability of both uni-meteorological variable (*e.g.*, air temperature only including Thornthwaite, 1948) and bi-meteorological variable (*e.g.*, air temperature and solar radiation such as Priestley and Taylor, 1972) formulations of ET_{pot} have increasingly been questioned (*e.g.*, Chen et al., 2005; Garcia et al., 2004; McKenney and Rosenberg, 1993; Shenbin et al., 2006). These researchers advocate use of physically based formulations of ET_{pot} (such as the Penman—Monteith approach that uses solar radiation, humidity and wind speed) as feedbacks between the forcing meteorological variables can influence the resulting ET_{pot} calculation. Given that mountainous regions may experience climate change more rapidly than adjacent lower areas (Beniston and Rebetez, 1996; Giorgi et al., 1997; Williams et al., 1996), it is imperative to use physically realistic expressions of ET_{pot} while considering topographic influences on forcing variables in such environments.

Our paper fills the niche of spatially distributing ET_0 (a physically based ET_{pot} formulation) while modelling the influence of topography and land-surface conditions on the forcing variables by using an 'interpolate-then-calculate' approach (McVicar and Jupp, 2002; Stein et al., 1991). Our approach maximises the temporal and spatial influence forcing variables have on the resulting ET_0 estimates because topographic influences in-between the meteorological stations (which is the vast majority of the study site) are considered. ET_0 has been shown to be sensitive to changes in forcing variables both temporally and spatially (Gong et al., 2006). Implementing an elevation dependent 'interpolate-then-calculate' approach uses information from many points (*e.g.*, millions — as topographic information is used as a covariate), whereas a geometric two dimensional 'calculate-then-interpolate' approach uses information from less points (*e.g.*, tens to hundreds). We note that the need to accurately include the influence of topography on resulting surfaces of ET_0 obviously depends on their use and spatial resolution. For example, the 25 km resolution data produced for the Yangtze River basin (Xu et al., 2006) was developed to assess spatio-temporal climatological patterns and trends, and hence the need to accurately account for topographic influences is likely less stringent. In contrast, our results are used to predict the impact of land use change on regional hydrology (McVicar et al., in press; Zhang et al., in press), and map perennial vegetation suitability (McVicar et al., 2005b), and hence higher resolution data accurately accounting for topographic influences in all forcing datasets are needed. Conse-

quently, the results, and methods used here to generate the results, are important as many communities across the globe rely on water resources derived from the headwaters of catchments that are often topographically complex. Thus developing physically reasonable methods to spatially distribute ET_0, or ET_{pot}, while considering the impact of topography on the forcing meteorological variables is important. The resulting surfaces (ET_0 or ET_{pot}) are also useful because they can be modulated by a moisture availability function to calculate actual evapotranspiration (ET_{act}) for use in water balance models (*e.g.*, Chiew and McMahon, 1992; Keig and McAPine, 1974; Wallace, 1995). In order to assess the reliability of the resulting ET_0 surfaces in our paper, pan evaporation (E_{pan}) was also spatially interpolated and from these a set of pan coefficient (K_{pan} — a unitless ratio defined as ET_0/E_{pan}) surfaces were calculated. Spatio-temporal analysis of the resulting ET_0, E_{pan} and K_{pan} surfaces were conducted for the entire study site and for a transect with large elevation differences. These results highlight the control topography has on meteorology, especially where aspect changes quickly. The remainder of the paper is organised as follows. In Section 'Study site' the input data are described with climatologies characterising the hydrometeorological environment provided. Section 'Methods' includes the following sub-headings: (i) select the spline model and determine the elevation relationships; (ii) spatially model the radiation environment; (iii) calculate ET_0; (iv) spatially interpolate E_{pan}; (v) calculate K_{pan}; (vi) assess the sensitivity of resulting evaporative forms to spatial interpolation; and (vii) characterise the influences of R_n, ET_0, and K_{pan} to both dynamic and static land surface parameterisations used in radiation modelling. Section 'Results and discussion' uses the same sub-headings as in Section 'Methods', and finally conclusions are made.

Study site

Major environmental issues

The Yellow River basin (752,444 km^2) in China is one of its most important basins, directly supporting a population of 107 million people with another 400 million living on the North China Plain (Fig. 1), who partly rely on water from this basin. The average annual erosion rate (2480 t km^{-2}) for the entire Yellow River basin is the highest of any major river system worldwide (Shi and Shao, 2000). This is caused by the middle reaches of the Yellow River draining the Loess Plateau (623,586 km^2 — Fig. 1), where severe soil erosion rates ranging from 20,000 to 30,000 t km^{-2} $year^{-1}$ are commonly reported (*e.g.* Xiang-zhou et al., 2004), though extremely high rates (59,700 t km^{-2} $year^{-1}$) have also been documented (Shi and Shao, 2000). Levees and dykes have been constructed over the past 2000 years on the lower reaches of the Yellow River to contain the river in times of flood (Ren et al., 1985). The high erosion rates from the Loess Plateau combined with continuous presence of levees and dykes means that in the lower reaches of the Yellow River (*i.e.*, on the North China Plain — Fig. 1), the bottom of the river bed is, in places, 20 m above the surrounding land surface (Li, 2003). Approximately 90% of the sediment delivered to the Yellow River comes from the
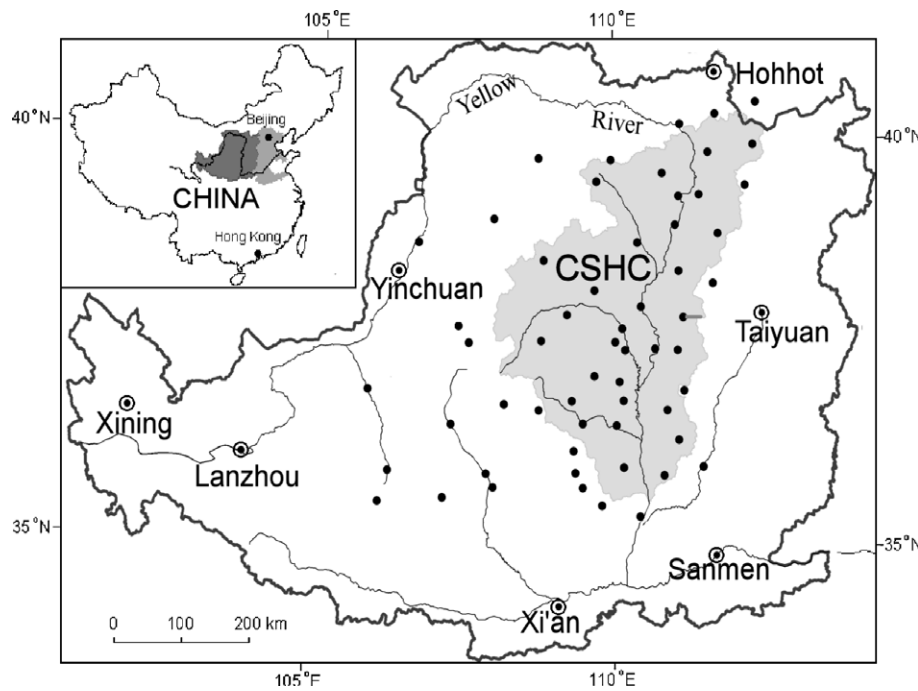
Figure 1 The inset map shows the location of the Loess Plateau (dark shading) and the North China Plain (lighter shading) on the middle and lower reaches of the Yellow River, respectively. The main map shows the location of the 112,728 km^2 Coarse Sandy Hilly Catchments (CSHC) where the dark grey line represents the boundary of the Loess Plateau. The location of the meteorological stations are shown by the black dots, and the location of a 23 km transect (in red) used in Fig. 12 is shown on the eastern border of the CSHC. (For interpretation of colour representation in this figure legend the reader is referred to the web version of this article.)

major south-flowing branch draining the region of the Loess Plateau, locally known as the 'sandy coarse-sandy area' (Li, 2003). Our study site is defined by the catchments encompassing this sandy area where the landform is primarily hilly and is thus termed the Coarse Sandy Hilly Catchments (CSHC, see Fig. 1).

To reduce this erosion, and its downstream impacts (Li, 2003), the Chinese Central Government has developed a ''National Forest Protection Project (NFPP)'' and under that umbrella the ''Grain for Green'' (Tui Geng Huan Lin) project was established with the aim to return cultivated land to forest (e.g., Ke and Zhou, 2005; Wenhua, 2004; Winkler, 2002; Xu et al., 2004; Yang, 2004; Ye et al., 2003). Since 1999, as part of the ''Grain for Green'' project over 7 million ha has been re-vegetated, with 5.9 million ha being converted in 2002 and 2003 alone (Xu et al., 2004). It is generally accepted that re-vegetating large areas of the landscape reduces streamflow, largely due to increasing rates of evapotranspiration (McVicar et al., in press; Sun et al., 2006; Xiubin et al., 2003). With approximately 43% of the annual runoff to the Yellow River basin generated from the middle reaches of the Yellow River (draining the Loess Plateau from Lanzhou to Sanmen, (Fig. 1), Li, 2003; Xiubin et al., 2003) and water resources being already overcommitted (e.g., Chen et al., 2003; McVicar et al., 2002; Varis and Vakkilainen, 2001; Xu et al., 2002) any reduction of streamflow generated from the Loess Plateau is a serious concern for the 500 million people partly reliant on its water. With average annual streamflow decreasing, and demand for water increasing, water resources will continue to be overcommitted into the future (Wallace, 2000; Xu et al., 2002).

Over the last 30 years the Yellow River has increasingly failed to reach the Bohai Sea (Li, 2003; Xiubin et al., 2003). This happened for the first time in recorded Chinese history in 1972 (for 15 days) and in 1997 (a 'drought' year) there were 226 zero-flow days; in the late 1990s the average number of zero-flow days per year was approximately 100 (Chen et al., 2003; Li, 2003). When zero-flow occurs all sediment is deposited in the river bed and this feedback exacerbates the rate at which the river bed increases its height above the surrounding plain.

Data description and characterisation

Monthly hydrometeorological data were obtained from January 1980 through December 2000 (21 years) from 58 stations in and around the CSHC; see Fig. 1. Detailed quality control was performed on the monthly data for all stations (Li et al., 2005a). Seven monthly hydrometeorological variables were recorded including: (1) mean maximum air temperature (T_{max} °C); (2) mean minimum air temperature (T_{min} °C); (3) mean wind speed (u m s^{-1}); (4) precipitation (P mm); (5) mean relative humidity (relative humidity %); (6) bright sunshine hours (n h); and (7) pan evaporation (E_{pan} mm). All measurements were made daily according to Chinese Bureau of Meteorology standards with monthly data being integrated or averaged from daily data as appropriate. While detailed definitions were reported in McVicar et al. (2005a) some issues need description here. Wind speed was measured from an anemometer located 10.0 m above the surface, and E_{pan} was the decline in water (precipitation corrected) from a 20-cm diameter by 10-cm deep

pan (called a micro-pan), that is filled to 2 cm, or sometimes 3 cm depending on local daily evaporative rates. Monthly relative humidity was converted to monthly vapor pressure (e_a) by calculating the saturated vapor pressure (e_s) at both T_{max} and T_{min} (e.g., Allen et al., 1998; McVicar et al., 2005a).

To characterise our study site, data measured at the 58 meteorological stations was spatially averaged to provide monthly values, and the time series of monthly data (252 months for the 21 years from 1980 through 2000) was subsequently temporally averaged to illustrate general characteristics (Fig. 2). As expected, both T_{max} and T_{min} peak in July (Fig. 2a and b). The monthly distribution of u is weakly bi-modal, with a strong peak in spring (April) and a weaker peak in late autumn (November), see Fig. 2c. The influence of the summer monsoons on P with most occurring in July and August is clearly seen (Fig. 2d). The general pattern of relative humidity (Fig. 2e) is governed by the summer monsoons. It increases during summer months peaking in August, and slowly declines until the minimum is experienced during the following autumn. Maximum n occurs in May (Fig. 2f); governed by the relative summer–winter day-length differences, modulated by increasing cloud cover associated with the summer monsoons. Fig. 2g shows that monthly E_{pan} is greater than 200 mm from April to August reaching almost 300 mm in May and reduces to approxi-

mately 40 mm in both December and January. Fig. 2h shows that maximum e_a is observed in summer (July and August) coincident with the summer monsoons and minimum e_a is experienced in winter. Fig. 2i shows that $e_s - e_a$ is low in winter, and increases rapidly during April and May, to reach its maximum value in June. As e_a is highest in July and August, $e_s - e_a$ starts to decrease during these months, and decreases linearly through the autumn months (September to November). Annual time series trends in our base meteorological data (McVicar et al., 2005a) are in agreement with those reported for all China (Liu et al., 2004; Shen and Varis, 2001; Wu et al., 2006; Zhai et al., 1999).

Methods

To spatially distribute ET_0 on a grid-cell basis required that the input variables were either spatially interpolated, or spatially modelled; these are discussed in turn in the next two sub-sections. Our ET_0 is slightly modified from that proposed by Allen et al. (1998) as we spatially distributed the input variables for the 252 months with as much physical reality as possible. This was performed by taking elevation into account when interpolating the hydrometeorlogical data, and accounting for topography (i.e., elevation, slope and aspect) and temporally varying land-cover based surface conditions when modelling the radiation environment.
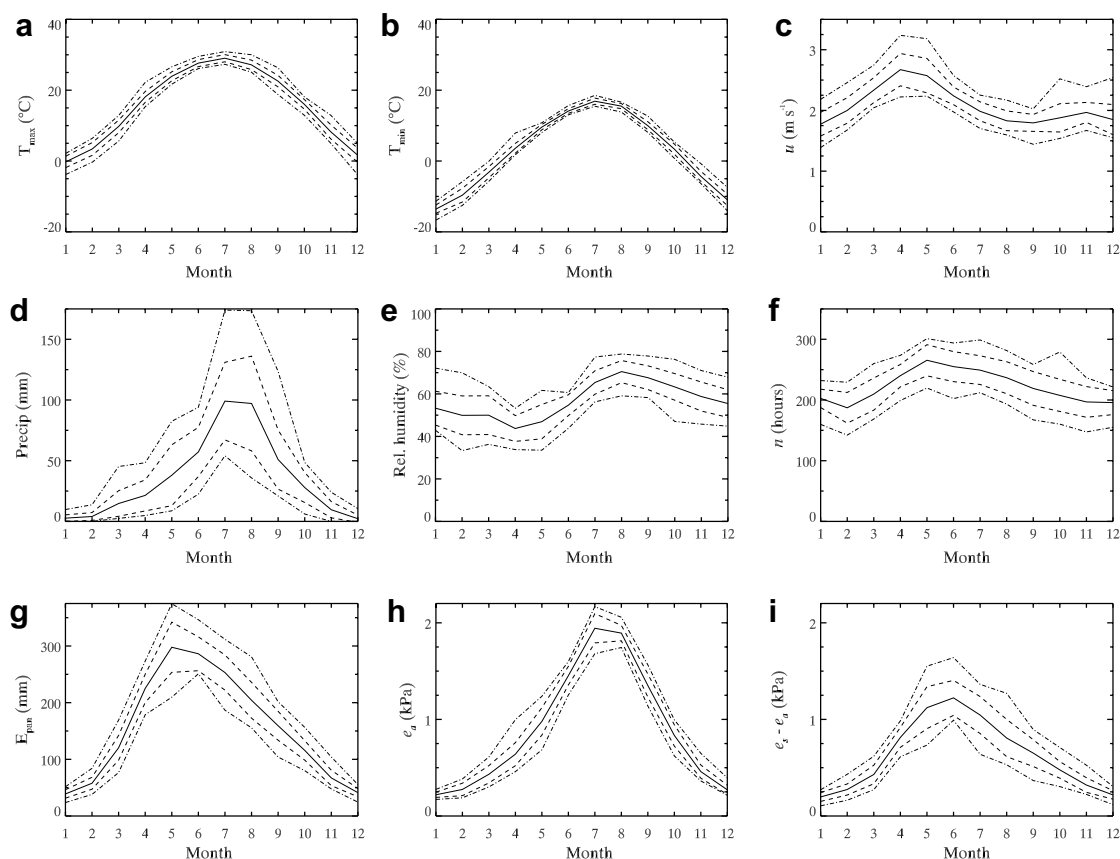

Figure 2 Monthly values of: (a) T_{max} (°C); (b) T_{min} (°C); (c) u (m s^{-1}); (d) P (mm); (e) relative humidity (%); (f) n (hours); (g) E_{pan} (mm); (h) e_a (kPa); and (i) $e_s - e_a$ (kPa). The 21-year mean (solid line), ± 1 standard deviation (dashed lines), and the minimum and maximum (dash–dot lines) are shown.

The outputs from the spatial interpolation and spatial modelling were then used in the FAO-56 ET_0 formulation — see Eq. (1).

There are many algorithms available to spatially interpolate data (Lam, 1983), with a few of these being primarily used to interpolate meteorological and climatic data sets (*e.g.*, Daly, 2006; Hong et al., 2005, and the references in each). Daly (2006) summarises the five main methods as: (1) inverse distance weighting; (2) various forms of kriging; (3) tri-variate splines implemented using ANUSPLIN; (4) local regression models (Daymet and PRISM are examples); and (5) regional regression models. In this research ANUSPLIN was used — our goal was not to compare different methods, and we recognise that each has relative strengths and weaknesses (Daly, 2006). Previous research has shown that results from splines, including ANUSPLIN, were favourable when compared with other interpolation algorithms (Price et al., 2000), including kriging (Hutchinson and Gessler, 1994; Laslett, 1994). For example, when interpolating precipitation in Canada, Price et al. (2000) reported that the ANUSPLIN root mean square error was lower than the Gradient plus Inverse-Distance Squared (GIDS) counterpart for all months in the mountainous British Columbia/Alberta region and for 10 months in the flatter Ontario/Québec region. Given that a previous comparison (Nalder and Wein, 1998) showed the superiority of GIDS over six other interpolation methods (including kriging), the results of Price et al. (2000) provide a strong argument for using ANUSPLIN. Additionally, ANUSPLIN has been used extensively for spatially interpolating hydrometeorological surfaces including: air temperatures (*e.g.*, Hong et al., 2005; Hutchinson, 1991; McVicar and Jupp, 2002); wind speed and wind run (*e.g.*, Hutchinson, 1989; Hutchinson et al., 1984b); vapor pressure (*e.g.*, Jeffrey et al., 2001; McVicar and Jupp, 2002); solar radiation and atmospheric transmittance (*e.g.*, Hutchinson et al., 1984a; Jeffrey et al., 2001; McVicar and Jupp, 2002); precipitation (*e.g.*, Hutchinson, 1995; McVicar et al., 2002; Price et al., 2000) and pan evaporation (*e.g.*, Jeffrey et al., 2001; Sharples et al., submitted for publication).

Wahba and Wendelberger (1980) primarily developed thin-plate spline interpolation, with Wahba (1990) extending the theoretical development to include covariates (or parametric sub-models), the resultant model being termed a partial thin-plate spline. Hutchinson (1991); Hutchinson (2004b) has implemented these algorithms in ANUSPLIN, primarily to spatially interpolate hydrometeorological and climatological variables; it provides a dependence on covariates (which can include elevation but is not limited to this) and methods for detecting data errors. ANUSPLIN reports several statistics including the expected true mean-square error, $T(m,\lambda)$, which is regarded as an optimistic measurement of error and the generalised cross-validation statistic, $GCV(m,\lambda)$ considered a pessimistic, or conservative, measurement of error (Hutchinson, 2004b). When both errors are reported as a square root they have the units of the dependent variable. The order of the spline (m) and the smoothing parameter (λ) control the trade-off between the amount of data fidelity and surface roughness (Hutchinson, 1991). λ is determined by minimising the $GCV(m,\lambda)$ which has been previously used to find the 'best' model among competitors (Davis, 1987).

Spatially interpolating the required meteorological variables

Selecting spline models

To select the variable-specific ANUSPLIN parameters, the year with near-average annual precipitation was selected (as most other hydrometeorological variables are somewhat positively or negatively correlated to precipitation). The annual mean for the 58 stations was 421 mm and as 1995 had a spatially-averaged value of 424 mm, this year was selected as the test year. When interpolating T_{max}, T_{min}, u, e_a, and P, 18 spline models were explored. The 18 variants were slight modifications on three main spline models; they were:

(1) bi-variate thin plate spline (BVTPS) as a function of longitude and latitude only;
(2) tri-variate partial thin plate spline (TVPTPS) incorporating a BVTPS as a function of longitude and latitude and a constant linear dependence on elevation; and
(3) tri-variate thin plate spline (TVTPS) as a function of longitude, latitude and elevation, with the units of elevation varying from km to cm.

Elevation was provided with the location of the meteorological stations, and this was in agreement with the hydrologically correct Digital Elevation Model (Yang et al., in press; Yang et al., 2005) developed using ANUDEM (Hutchinson, 2004a) that was used as the covariate when developing the output surfaces. When using a TVPTPS there is no sensitivity to the relative scaling of elevation. However, if implementing a TVTPS it has been shown that the range of the three variables (usually controlled by a relative scaling of elevation) should be approximately equal (Hutchinson, 1995). In this research we use an Albers projection with the units of metres and the relative scaling of elevation when using a TVTPS is provided in units of km, m, dm and cm (McVicar et al., 2005a). In all cases, (1) to (3) above, m was set at 2, 3, and 4. As both P and u can have positively skewed distributions, the impact of using a square root transformation prior to fitting the data with a spline was assessed (Hutchinson, 1995).

Previous modelling of atmospheric transmission has revealed that the diurnal temperature range is a good measure of atmospheric transmission (*e.g.*, Bristow and Campbell, 1984; McVicar and Jupp, 1999; Meza and Varas, 2000). Hutchinson et al. (1984a) used a transformation of monthly precipitation as an index of cloudiness, which can be otherwise thought of as an indicator of atmospheric transmission. Given this, we examined both the monthly air temperature range (ΔT) and/or P as additional variables (either independent variable or covariates) when fitting n. All eight possible combinations were evaluated with m being 2, 3 or 4 — hence 24 spline models were tested. Full details are provided in McVicar et al. (2005a).

For each variable, to temporally assess the relative error for the 252-month sequence both the pessimistic expression of relative error ($\sqrt{GCV(m,\lambda)}$) and the more optimistic expression of relative error ($\sqrt{T(m,\lambda)}$) were divided, in turn, by the observed standard deviation (SD) for each month.

Analysis of elevation dependencies

Several of the variables were interpolated with a TVPTPS using elevation as a covariate (see Section 'Results and discussion'). In this case a constant linear dependence (or constant sub-model) is determined as a function of elevation when fitting the data. For T_{max} and T_{min} this is known as the lapse rate. For other meteorological variables influenced by elevation, most notably u and e_a, this metric is termed the near-surface elevation-dependence (NSED). For each variable the average monthly NSED value was calculated from the 252-month sequence. As the NSED for T_{max}, T_{min} and e_a are usually negative, using the terms 'increase' or 'decrease' can be confusing (Pepin and Losleben, 2002; Pepin, 2000), so following their protocol for these three variables (and using T_{max} as an example) herein a 'steeper' NSED means a more negative lapse rate and a 'shallower' NSED denotes a less negative lapse rate. For u, where the NSED is commonly positive, the terms 'stronger' (and 'weaker') will be used to mean an increasing (or decreasing) NSED, respectively. If elevation (x-axis) was cross plotted against T_{max} (y-axis) the lapse rate is the slope of this relationship and using a spline allows the offset of this relationship to vary spatially. Regression modelling does not allow this offset to vary spatially and this is a major distinction between spatially implementing regression models and using a spline model.

Spatially modelling the radiation environment (R_n and G)

To calculate ET_0 both R_n and G were spatially modelled. R_n is the balance of the incoming and outgoing shortwave and longwave radiation components defined by:

$$R_n = R_{s\_in} - R_{s\_out} + R_{l\_in} - R_{l\_out} \qquad (2)$$

where: R_{s_in} (MJ m^{-2} day^{-1}) is the incoming (or solar) shortwave (0.15–4 µm) radiation measured on a horizontal surface; R_{s_out} (MJ m^{-2} day^{-1}) is the shortwave radiation reflected by the surface, governed by the surface albedo (α); R_{l_in} (MJ m^{-2} day^{-1}) is the incoming longwave radiation (>4 µm); and R_{l_out} (MJ m^{-2} day^{-1}) is the longwave radiation emitted from the surface into the atmosphere.

We used SRAD (an abbreviation for Solar RADiation) on a 12-minute time-step to model all processes governing the radiation environment in complex terrain (McKenney et al., 1999; Moore et al., 1993; Wilson and Gallant, 2000). SRAD uses the Ångström–Prescott equation (Prescott, 1940), which is based on the ratio of n to total sunshine hours (N) as its measure of atmospheric transmittance. Historical developments of the Ångström–Prescott formula, and its many variants, are reviewed by Martinez-Lonano et al. (1984) and Ulgen and Hepbasli (2004). The original Ångström–Prescott equation has the form:

$$R_{s\_in} = \left(a + b\frac{n}{N}\right)R_a \qquad (3)$$

where R_a is the extraterrestrial (or top-of-Earth atmosphere) solar radiation measured on a horizontal surface (MJ m^{-2} day^{-1}); a and b are semi-empirical coefficients; a being the atmospheric transmittance relating R_{s_in} to R_a for totally overcast days (i.e., when $n = 0$); and $a + b$ being the atmospheric transmittance for totally clear days (i.e., when $n = N$).

With n being spatially interpolated, N was calculated for the 15th day of each month, using Allen et al.'s (1998) method, and then multiplied by the number of days in each month. For each of the 252 months surfaces of n/N, T_{max}, T_{min} and e_a were input to SRAD. Several other parameters were required (Wilson and Gallant, 2000), including the Ångström–Prescott a and b coefficients. If no local measurements are available, it is suggested to use $a = 0.25$ and $b = 0.5$ (Allen et al., 1998). Recently Chen et al. (2004) reported a and b values for China and here we used the average of the four closest stations (Xian, Lanzhou, Yinchuan and Taiyaun) from their research; the mean values for a and b were 0.195 and 0.5125, respectively. While these values are slightly lower than Allen et al.'s (1998) suggested values, they are in agreement with other radiation modelling that has shown that atmospheric transmittance in China is low (Lin and Lu, 1998; McVicar and Jupp, 1999), due to high amounts of aerosols.

R_{l_in} was calculated using $\varepsilon_a \sigma T^4 + (1 - v)R_{l\_out}$ where ε_a is the effective atmospheric emissivity (Prata, 1996); σ is the Stefan–Boltzmann constant (5.67×10^{-8} W m^{-2} K^{-4}); and v is the sky view factor for each grid cell (driven by slope and horizons of each grid cell, Moore et al., 1993). R_{l_out} was calculated as $\varepsilon_s \sigma T^4$ where ε_s is the surface emissivity given as 0.96. In SRAD, slight modification of T_{max} used to calculate T was made to capture the influence of aspect and vegetation density, given by Leaf Area Index (LAI) (Hungerford et al., 1989; Moore et al., 1993; Running et al., 1987). To model R_n with as much physical reality as possible both LAI and α were provided as land-cover dependent time series for use in SRAD. This was the basis of our slight modification of ET_0 — meaning that the FAO-56 ET_0 formulation (Eq. (1)) was used with spatially distributed inputs that were as physically realistic as possible. Both LAI and α were defined for 1:500 000 scale polygons of land-cover classes derived from Landsat Thematic Mapper data acquired in 1986 (Shen, 1991). The 8 main land-cover classes were: (1) agriculture; (2) forest; (3) sparse forest; (4) shrubland; (5) pasture; (6) urban; (7) water; and (8) desert — see McVicar et al. (2005a) for the locations. The logic of the temporally varying LAI and α parameters used in SRAD for the 8 main land-cover classes is provided below.

Summer crops are planted in April, rapidly growing in June and July reaching their maximum LAI in August with LAI rapidly decreasing during the reproductive stage prior to senescence (Mo et al., 2004; Wu et al., 2003). In winter agricultural LAI is negligible (Zhu et al., 1999), yet considering that the minimum mapping unit of the 1:500 000 scale land-class data will be a mix of different land-covers (including small patches of forest), agricultural LAI never falls below 0.5 in the SRAD parameterisation. The forest and sparse forest land-covers are a mixture of evergreen conifers and deciduous broadleaf forest communities (Liang et al., 2003). LAI increases from winter to summer due to the phenology of the deciduous species, and during summer there will also be a slight increase of LAI as understorey perennial grasses grow. Values from Mo et al. (2004, their Table 1) were used to parameterise the forest and sparse forest LAI time series; they provide minimum LAI for evergreen conifers and deciduous broadleaf of 3.0 and 0.5, respectively. Shrubland also contains evergreen and deciduous species (Liang et al., 2003). In general, its overstorey

canopy closure is less than forested lands (Wu et al., 2003), meaning there will be a greater effect of the grass understorey on shrubland in summer compared to forest in the same season (Table 1). Pasture reaches its maximum LAI earlier than the agricultural crops and remains at a LAI of 3.0 for the remainder of summer, slowly decreasing and remaining low over winter (Wu et al., 2003). Urban areas have isolated trees, and hence have a constantly low LAI. Water areas were assigned a LAI of 0.0 and desert areas (or 'wasteland' Wu et al., 2003) were assigned a value of 0.5 in winter increasing to 1.0 in the wetter summer months (July and August) when perennial grasses will respond to more favourable conditions (see Table 1).

The α of water was set at the average value of the water class provided by Brutsaert (1982). For the remaining classes α was determined by recognising that, at low LAI, the land-cover α is dominated by the soil α and, when the LAI $\approx \geqslant 3.0$ (depending on the canopy architecture), land-cover α is primarily dominated by the vegetation α (Stanhill, 1970). In the Loess Plateau soil α is high with values ranging from 0.28 to 0.35 (Li et al., 2000; Li et al., 2002; Qiang and Ronghui, 2004). Li et al. (2000) show that land-surface α decreases as the percent vegetation cover increases, as soil α is typically higher than the vegetation α. Since grazing density is unknown at the temporal and spatial extents of the study site, for pastures we used the moderately grazed values reported by Li et al. (2000) as the basis for parameterisation. Deserts were assumed to have 10% vegetation cover during winter which increases slightly over summer causing a corresponding slight decrease in α (Table 2). For agriculture, it was assumed that the winter α would be the average of the desert α (0.30) and the pasture α (0.28), as we expect

more fallow in agricultural areas. The minimum α of 0.23 (Allen et al., 1998) is assumed to occur at the time of maximum LAI, with crop phenology dictating the representative temporal change in α for agriculture (Mo et al., 2004). Brutsaert (1982) reported approximate ranges of α for evergreen conifers (0.1–0.15) and deciduous broadleaf trees (0.15–0.25); these values were used with the knowledge that LAI for forest > sparse forest > shrubland to provide monthly estimates of α for these three land-cover classes. Due to differing amounts of vegetation cover, and with vegetation having lower α than soil, comparative results for monthly α are forest < sparse forest < shrubland (Table 2). For each class (except urban and water), inter-annual α changes are governed by assumed increases of perennial growth associated with summer *P*. As with the monthly land-cover-specific LAI parameterisation, these monthly land-cover-specific α values represent generalised relationships as many factors (*e.g.*, climate variability, different species composition, grazing pressures of domestic and feral animals and insects) may cause slightly different actual time-traces for specific locations over the 21 years.

Following Allen et al. (1998), *G* was calculated as $0.07(T_{i+1} - T_{i-1})$ for each month *i* in the 252-month sequence. This assumes a constant soil heat capacity of 2.1 MJ m^{-3} °C^{-1}, and with the deep (50–200 m thick) unconsolidated silty loam soils present on the Loess Plateau (Huang, 1988), the actual soil depth is greater than the modelled soil depth beyond which soil temperature does not vary (approximately 2 m for a monthly time-step Allen et al., 1998). Daily output values of R_n and *G* were then multiplied by the number of days in each month to convert their units to MJ m^{-2} month^{-1} for use in the subsequent modelling.

Table 1 Indicative monthly LAI values for the 8 main land-cover classes used in SRAD

Class	Month											
	January	February	March	April	May	June	July	August	September	October	November	December
Agriculture	0.5	0.5	0.5	0.5	1.0	1.5	3.0	4.0	2.0	1.0	0.5	0.5
Forest	2.0	2.0	2.25	2.75	3.0	3.10	3.25	3.25	3.10	2.5	2.0	2.0
Sparse Forest	1.5	1.5	1.75	1.75	2.0	2.25	2.50	2.50	2.25	1.75	1.5	1.5
Shrubland	0.75	0.75	1.0	1.0	1.0	1.25	1.50	1.50	1.25	1.0	0.75	0.75
Pasture	0.5	0.5	0.5	1.0	2.0	3.0	3.0	3.0	3.0	2.0	1.0	0.5
Urban	0.2	0.2	0.2	0.2	0.2	0.2	0.2	0.2	0.2	0.2	0.2	0.2
Water	0.0	0.0	0.0	0.0	0.0	0.0	0.0	0.0	0.0	0.0	0.0	0.0
Desert	0.5	0.5	0.5	0.5	0.5	0.75	1.0	1.0	0.75	0.5	0.5	0.5

Table 2 Indicative monthly α values for the 8 main land-cover classes used in SRAD

Class	Month											
	January	February	March	April	May	June	July	August	September	October	November	December
Agriculture	0.29	0.29	0.29	0.29	0.27	0.26	0.24	0.23	0.25	0.27	0.29	0.29
Forest	0.15	0.15	0.15	0.15	0.15	0.145	0.14	0.14	0.145	0.15	0.15	0.15
Sparse Forest	0.18	0.18	0.18	0.18	0.18	0.17	0.16	0.16	0.17	0.18	0.18	0.18
Shrubland	0.20	0.20	0.20	0.20	0.20	0.19	0.18	0.18	0.19	0.20	0.20	0.20
Pasture	0.28	0.28	0.28	0.27	0.26	0.25	0.24	0.23	0.25	0.26	0.27	0.28
Urban	0.25	0.25	0.25	0.25	0.25	0.25	0.25	0.25	0.25	0.25	0.25	0.25
Water	0.06	0.06	0.06	0.06	0.06	0.06	0.06	0.06	0.06	0.06	0.06	0.06
Desert	0.30	0.30	0.30	0.30	0.30	0.29	0.28	0.28	0.29	0.30	0.30	0.30

Calculating ET_0

The 252 monthly surfaces of ET_0 were calculated for each month independently on a grid-cell basis using an 'interpolate-then-calculate' approach with the outputs from the spatial interpolation and spatial modelling conducted above used as inputs. This means that changes in forcing variables as a function of: (1) seasonality; (2) topography (including elevation, slope and aspect); (3) climate variability; and (4) longer term trends (associated with climate change) are implicitly accounted for when spatially distributing the required variables needed to calculate ET_0. Near-surface u interpolated surfaces were based on measurements made 10.0 m above the ground. A wind-profile relationship was applied to generate u 2.0 m above the ground (u_2); this was $u_2 = u_z \frac{4.87}{\ln(67.8z - 5.42)}$ (Allen et al., 1998); where z is 10 m. e_s was calculated (Allen et al., 1998) from the surfaces of T_{max} and T_{min}, and with e_a being spatially interpolated, $e_s - e_a$ was calculated on a grid-cell basis; representative examples are shown in McVicar et al. (2005a). Using methods outlined in Allen et al. (1998) Δ and γ were calculated; see McVicar et al. (2005a).

Spatially Interpolating E_{pan}

In cases where all meteorological data needed to calculate ET_0 are not available, it is common to use E_{pan} for periods of 10 days or longer as a surrogate for ET_{pot} (Allen et al., 1998). Obviously, ET_0 and E_{pan} are not identical expressions of the potential amount of liquid water that may be transformed into the gaseous phase; they have historically been related through the empirically defined pan coefficient (K_{pan}), which is a unitless ratio defined as ET_0/E_{pan}. To assess the reliability of the ET_0 surfaces, measurements of E_{pan} made at the network of meteorological stations in and around the CSHC were spatially interpolated. To perform this interpolation while capturing as much of the governing physical processes as possible meant that dependent (co)variables additional to longitude and latitude needed to be tested — the three candidates examined were $e_s - e_a$, R_n, and u. These three variables, and only these three, were assessed due to their use in previous E_{pan} models (Rotstayn et al., 2006; Thom et al., 1981) that account for the radiation and aerodynamic components and are most suited to geographic distribution. For monthly estimates of E_{pan}, the influence of changes of heat storage in the pan (a function of the pan water temperature which would lag changes in air temperature) is negligible (Roderick and Farquhar, 2005; Thom et al., 1981); hence T is not explored as a potential covariate here. The utility of each of the three candidate dependent (co)variables was first explored by linear regression, using multiple linear regression as required, against measurements of E_{pan}. After deciding which (co)variables to use surfaces of E_{pan} were generated using ANUSPLIN (as opposed to spatially implementing a regression model) as ANUSPLIN allows offsets to be spatially variable (which regression models do not). McVicar and Jupp (2002) previously employed the approach of first using regression models to decide which candidate dependent (co)variables are subsequently used to spatial distribute an independent variable using ANUSPLIN.

Table 4 shows that using all three potential dependent (co)variables has the highest r^2 and lowest root squared difference (RSD) statistics from the six possible combinations, so we decided to develop quint-variant (longitude, latitude, $e_s - e_a$, u, and R_n) spline models to spatially interpolate E_{pan}. However, it was unclear if the spline model should be a function of these three additional variables or if constant linear dependencies using the three additional variables as sub-models (or some combination of the two) should be developed. McVicar et al. (2005a) tested all eight possible options, and for each, m was set at 2, 3 or 4 — hence 24 spline models were tested. Once a model was selected and used for the 252-month sequence, the two temporal assessments of the relative error: (1) the pessimistic expression $\sqrt{GCV(m, \lambda)}/\text{SD}$; and (2) the optimistic formulation $\sqrt{T(m, \lambda)}/\text{SD}$ were calculated on a monthly time-step.

Calculating K_{pan}

Values of K_{pan} vary depending on, among other factors, local meteorological conditions, local landscape position, type of pan, and maintenance of the pan. Long-term site factors also need to be considered: trees growing close to meteorological stations can reduce u and there can be changes in the radiative environment (Roderick, 2006; Stanhill and Cohen, 2001) that also produce changes in E_{pan} measurements (Thom et al., 1981) and thereby influence K_{pan}. Nevertheless, analysing the spatial and temporal trends of K_{pan} provides a means to assess the representativeness of both ET_0 and E_{pan} as spatially distributed measures of E_{pot}. Given this, 252-monthly surfaces of K_{pan} were calculated simply by dividing ET_0 by E_{pan}, i.e., $K_{pan} = ET_0/E_{pan}$. For the 23-km transect located in Fig. 1 these three variables were extracted from the resulting surfaces and monthly means were calculated for each 100 m grid-cell along the transect.

Sensitivity analysis of ET_0, E_{pan} and K_{pan} to spatial interpolation

To characterise sensitivity, comparisons were made between: (1) calculations (or measurements in the case of E_{pan}) made with data measured at stations; and (2) values extracted from the output surfaces of the spatial interpolation/spatial modelling. For the 3 variables (denoted Var in the following being ET_0, E_{pan} or K_{pan} in turn) four statistics were generated between the calculated (denoted $\text{Var}_{\_c}$) and extracted (identified by $\text{Var}_{\_e}$) values. They are:

$$\text{Root Squared Difference (RSD)} = \left[\frac{1}{\text{num}} \sum_{j=1}^{\text{num}} (\text{Var}_{\_c} - \text{Var}_{\_e})^2 \right]^{\frac{1}{2}};$$

$$\text{Bias} = \frac{1}{\text{num}} \sum_{j=1}^{\text{num}} (\text{Var}_{\_c} - \text{Var}_{\_e});$$

$$\text{Relative RSD} = \left[\frac{1}{\text{num}} \sum_{j=1}^{\text{num}} (\text{Var}_{\_c} - \text{Var}_{\_e})^2 \right]^{\frac{1}{2}} \Big/ \text{Var}_{\_c}; \text{ and}$$

$$\text{Relative Bias} = \left[\frac{1}{\text{num}} \sum_{j=1}^{\text{num}} (\text{Var}_{\_c} - \text{Var}_{\_e}) \right] \Big/ \text{Var}_{\_c}.$$

(4)

These statistics were calculated using each of the 30 stations ($j = 1$ to num) located within the study site. Note the other 28 stations are located outside the CSHC, this ensures we are interpolating between stations for the entire CSHC and not extrapolating at its edges. For all monthly averages the starting point was a 7560 element array (12 months at 30 stations for 21 years) that was first averaged for the 21 years, and then for the 30 stations. Performing calculations in this order meant that extreme values, possibly seen at the edge of the study site where the interpolation is likely to be poorest, due to a relatively low density of input data, would be maintained in the resulting maximum and minimum statistics.

Sensitivity analysis of R_n, ET_0, and K_{pan} to land surface parameterisation

To assess sensitivity in land surface parameterisation when modelling R_n with SRAD, and as it propagates to ET_0 and K_{pan}, comparisons were made for all 3 variables between: (1) estimates made using temporally dynamic land-cover dependent LAI and α parameters (see Section 'Spatially modelling the radiation environment (R_n and G)'); and (2) values of the same 3 variables when LAI and α were static for each month and land-cover. Following Allen et al. (1998), the LAI and α were set to 2.88 and 0.23, respectively for the static case. For the 3 variables (denoted Var in the following being R_n, ET_0, or K_{pan} in turn) two statistics were generated between the dynamic (denoted Var$_{dynamic}$) and static (identified by Var$_{static}$) values. They are:

$$\text{Bias} = \frac{1}{\text{num}} \sum_{k=1}^{\text{num}} (\text{Var}_{dynamic} - \text{Var}_{static}); \text{ and}$$

$$\text{Relative bias} = \left[\frac{1}{\text{num}} \sum_{k=1}^{\text{num}} (\text{Var}_{dynamic} - \text{Var}_{static}) \right] / \text{Var}_{dynamic}.$$

$$(5)$$

Twelve monthly averages of each Var (both dynamic and static) were calculated first, and then Eq. (5) was implemented, and finally mean and variance statics were determined monthly for $k = 1$ to num, where num is the 11,272,796 grid-cells in the study site.

Results and discussion

Spatially interpolating meteorological variables

Selecting spline models
For T_{max}, T_{min}, u and e_a a TVPTPS provided the lowest errors and were primarily used to interpolate the data for the 21 years. For u the non-transformed results provided lower error than the square root transformed results. For n a TVPTPS using ΔT as a covariate was selected. For P, a BVTPS usually provided the lowest error statistics and so was selected. This result for P was unexpected, and while elevation is one controller of P it is also known that the distribution of P is highly discontinuous with many complex interacting factors governing its spatial and temporal distribution (Bergeron, 1960; Roe, 2005). This unexpected result is site and data specific, in that at the CSHC it appears that the influence of highly localised relative relief on P is not adequately captured by

the network of stations measuring P and unresolved topographic bias (Briggs and Cogley, 1996) results in tri-variate models (i.e., those using elevation as a dependent (co)variate) having larger errors than bi-variate models. The square root transformation of P (thereby making the positively skewed distribution more normal prior to fitting the spline) provided lower (or equal) error estimates when compared to non-transformed data (McVicar et al., 2005a), confirming the finding of Hutchinson (1998). Full details are presented in McVicar et al. (2005a), as are surfaces for all interpolated variables representing seasonal differences in 1995.

Results from assessing the relative error for the 252 month sequence for all 6 spatially interpolated variables, determined by dividing $\sqrt{GCV(m, \lambda)}$ and $\sqrt{T(m, \lambda)}$ by the observed SD for each month are presented in Table 3; with time series plots being provided in McVicar et al. (2005a). For T_{max} the temporal expression of relative error was smaller than T_{min} revealing that interpolating T_{min} was more challenging than T_{max}, most likely a result of nocturnal (or 'cold') air drainage (Bolstad et al., 1998; Gustavsson et al., 1998; Stull, 1988) in the topographically complex study site. Table 3 shows that T_{max} could be interpolated with low relative error, and that both T_{min} and e_a had moderate relative error, with u, n and P having relatively higher errors.

Analysis of elevation dependencies
When fitting data with a TVPTPS, using elevation as a covariate, ANUSPLIN calculates the NSED using all input data. Monthly mean (or monthly climatology) T_{max} lapse rates varied from $-3.01\ °C\ km^{-1}$ in winter to $-7.69\ °C\ km^{-1}$ in summer (Fig. 3a), with T_{min} lapse rates ranging from $-2.79\ °C\ km^{-1}$ in winter, to $-6.63\ °C\ km^{-1}$ in summer (Fig. 3b). These findings in terms of: (1) the magnitude; (2) T_{max} lapse rates being steeper than T_{min} lapse rates; and (3) for both T_{max} and T_{min} winter lapse rates being shallower than the summer counterparts are consistent with previous results for China (Chuanyan et al., 2004; Hong et al., 2005; Zhang and Lin, 1992), eastern USA (Bolstad et al., 1998), northwestern USA (Lookingbill and Urban, 2003; Thornton et al., 1997), and four sub-areas of the European Alps (Rolland, 2003).

It is widely known that near the crest of hills, near-surface u increases as elevation increases (Miller and Davenport, 1998; Wood, 2000); it has previously been termed 'wind speed-ups' (Miller and Davenport, 1998) and 'fractional speed-up ratio' (Taylor, 1998). This phenomenon has been previously reported for mountainous areas in China (Zhang and Lin, 1992). Note, we determine the NSED of u using measurements of u consistently made 10 m above the ground surface, so it is not the increase in u associated with reduced drag as altitude above the surface increases. The monthly climatology of NSED of u shows a marked seasonality with the control of elevation being stronger in winter than summer (Fig. 3c). In summer, when solar loading is highest, mesoscale convective circulation will be the dominant process controlling u in the boundary-layer (Kossmann et al., 1998), whereas in winter, synoptic frontal-scale winds dominate (Zhang and Lin, 1992) allowing greater influence of surface topography (both shape and elevation) resulting in a larger NSED of u. In the topographically complex country Switzerland, Weber and Furger (2001) showed

Table 3 For each of the 6 variables that were spatially interpolated, the mean, SD, maximum (Max.) and minimum (Min.) for the 252-monthly sequence of $\sqrt{GCV(m,\lambda)}/SD$ and $\sqrt{T(m,\lambda)}/SD$ are provided. All values are unitless fractions

	$\sqrt{GCV(m,\lambda)}/SD$				$\sqrt{T(m,\lambda)}/SD$			
	Mean	SD	Max.	Min.	Mean	SD	Max.	Min.
T_{max}	0.25	0.05	0.49	0.14	0.11	0.02	0.23	0.06
T_{min}	0.53	0.10	0.84	0.33	0.19	0.04	0.29	0.11
u	0.80	0.06	0.96	0.65	0.33	0.02	0.38	0.28
P	0.60	0.18	1.22	0.10	0.26	0.08	0.50	0.01
e_a	0.34	0.10	0.74	0.16	0.14	0.04	0.37	0.07
n	0.67	0.19	1.16	0.29	0.28	0.08	0.52	0.01

how the climatology of near-surface u is related to well known processes controlling flow patterns that have distinct mean u. Previously, no climatology on a monthly time-step of NSED of u has been reported, though for China Zhang and Lin (1992, pp 206) reported an annual mean NSED of u of 2.22 m s^{-1} km^{-1} for 6 station-pairs, where one station of each pair is located near the summit of high mountains. While their value is higher than our annual mean of 1.33 m s^{-1} km^{-1} (SD = 0.40 m s^{-1} km^{-1}) they only use 6 station-pairs with large elevation differentials where this phenomena would be exaggerated.

The monthly climatology of NSED for e_a is much steeper during summer than winter (Fig. 3d). The annual average of NSED for e_a (calculated by averaging the monthly means) is −0.333 kPa km^{-1} (SD = 0.205 kPa km^{-1}). Zhang and Lin (1992, pp 148), reported values ranging from −0.4 kPa km^{-1}

to −0.25 kPa km^{-1}, with a mean value of −0.337 kPa km^{-1} (SD = 0.055 kPa km^{-1}); our annual average NSED for e_a is similar. In agreement with results presented in Fig. 3d, for the contiguous United States, Dodd (1965) reported the dew point for proximally located station-pairs with substantial elevation differences. The monthly variation, calculated as the average value for three station-pairs is January (−0.176 kPa km^{-1}); March (−0.214 kPa km^{-1}); May (−0.303 kPa km^{-1}); July (−0.515 kPa km^{-1}); September (−0.416 kPa km^{-1}); and November (−0.239 kPa km^{-1}). Dodd (1965) illustrated that the NSED for e_a is steepest in summer (July) and shallowest in winter (January); the magnitude and this temporal pattern agrees with results shown in Fig. 3d.

The spline-generated underlying spatially variable offset for elevation−T_{max} cross plots are illustrated for 1995 for winter (February) and summer (August), see Fig. 4a and b
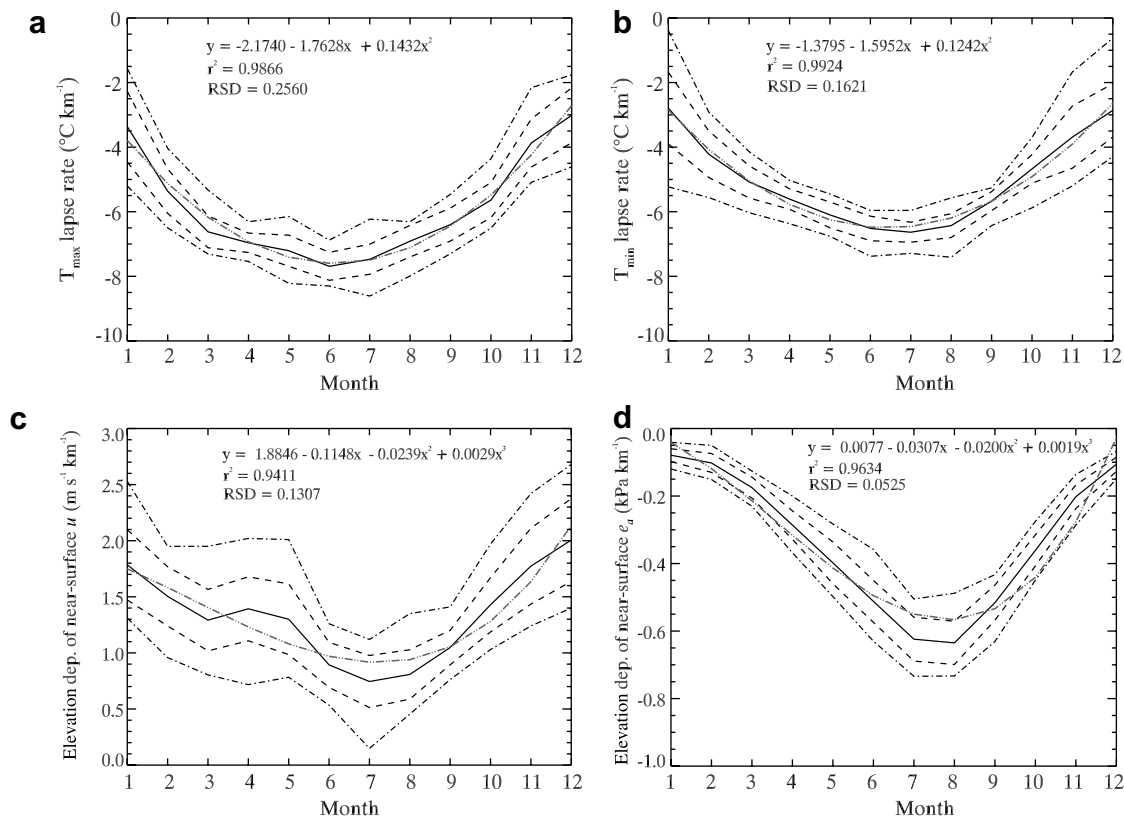

Figure 3 Monthly values of the NSED for: (a) T_{max}; and (b) T_{min}; (c) u; and (d) e_a. The 21-year mean (solid line), ±1 standard deviation (dashed lines), and the minimum and maximum (dash−dot lines) are shown. Lines of best fit (as a function of month number) are shown by grey (dash-dot-dot-dot) lines, with equations and statistics of fit provided on each plot.
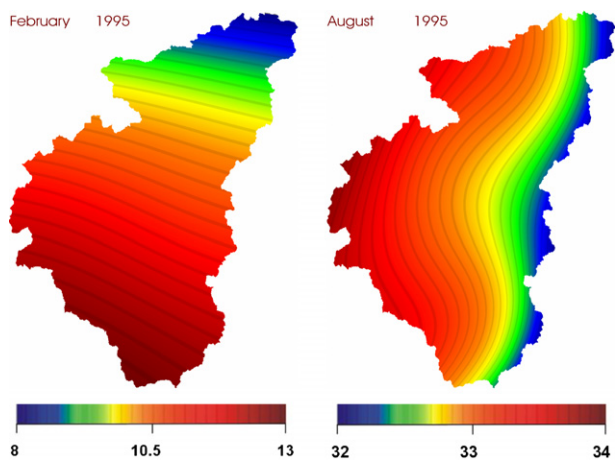
Figure 4 Spatially varying offsets of the elevation—T_{max} relationship are shown; units are °C.

respectively. These surfaces are generated as if there was no surface elevation present. For February (Fig. 4a) the pattern is primarily north—south and is driven by solar loading, while for August (Fig. 4b) a strong east—west signal governed by the differential moisture associated with monsoon rains influenced by the continentality effect is seen. These figures illustrate the worth of using splines to spatially distribute hydrometeorological data over spatially implementing regression models. Of course for forcing data used here, and in subsequent calculations, surface elevation (as appropriate) was used to generate the data; example surfaces for all interpolated variables representing seasonal differences in 1995 are presented in McVicar et al. (2005a).

Spatially modelling the radiation environment (R_n and G)

Surfaces of R_n and G were calculated for the 15th day of each month for the 252-month sequence, with monthly mean daily values for the entire study site from the 21-years provided in Fig. 5. These values are obtained by spatially averaging the resultant surfaces, and then temporally averaging those values. For R_n on a per grid-cell basis the minimum of

-4.85 MJ m^{-2} day^{-1} was estimated in November 1986 and the maximum of 21.06 MJ m^{-2} day^{-1} was simulated in July 1985. As expected, R_n reaches its maximum in summer, decreasing to its minimum in winter, and G being larger in spring (March and April) and lowest in autumn (October and November) when rates of change in T were largest.

Calculating ET$_0$

Per grid-cell monthly average surfaces of ET$_0$ for the 21 years (derived from 252 monthly surfaces) are shown in Fig. 6 where the strong seasonal trend of $e_s - e_a$ (following the onset of the summer monsoon and associated seasonal changes in T) and R_n are obvious. In winter (from November to February) some steep north-facing slopes have negative values of R_n, causing the resultant ET$_0$ values to be negative which is logically incongruous. Consequently, all grid-cells with negative ET$_0$ values have been nulled in all following calculations.

Fig. 7 shows the long-term monthly average of ET$_0$, and measures of variance around this average associated with climate variability. These values are obtained by spatially averaging the resultant surfaces, and then temporally averaging those values.

Spatially interpolating E_{pan}

Results presented in Table 4 show that E_{pan} and $e_s - e_a$ have the strongest relationship of the three meteorological variables tested. When adding the other variables, in turn, to $e_s - e_a$ and performing multiple linear regression, it can be seen that the results for $e_s - e_a$ and u are slightly better than those for $e_s - e_a$ and R_n (Table 4). Subsequently use of all three variables provides the best fit (as determined by the r^2 statistic) and the lowest error (as determined by the RSD statistic); see Table 4. This analysis was performed using monthly data for the 30 stations in the study site for 21 years; there were 7560 observations.

Of the 24 spline models tested, the quint-variate partial thin plate spline (QVPTPS) incorporating a BVTPS function of longitude and latitude with constant linear dependencies on $e_s - e_a$, u and R_n with $m = 2$ provided the lowest errors. This primary model was used for the majority of months, though
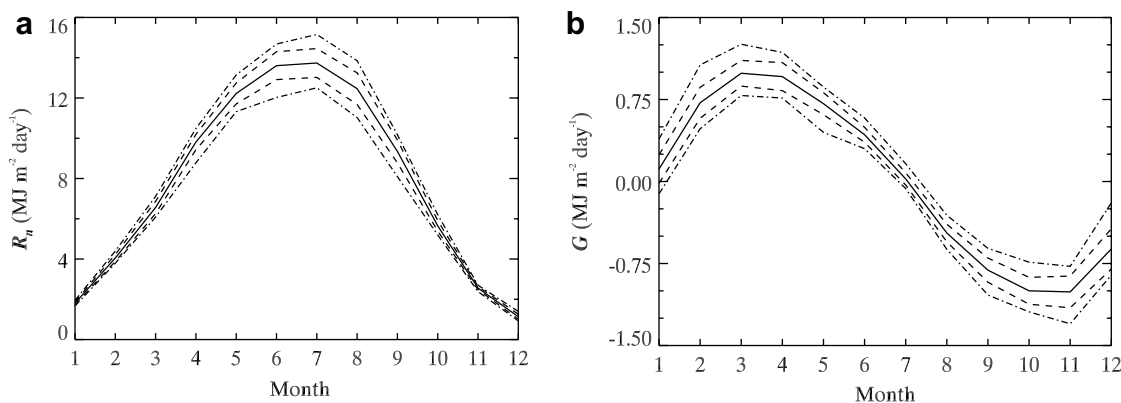

Figure 5 Monthly values of average daily: (a) R_n (MJ m^{-2} day^{-1}); and (b) G (MJ m^{-2} day^{-1}). The 21-year mean (solid line), ± 1 standard deviation (dashed lines), and the minimum and maximum (dash—dot lines) are shown.
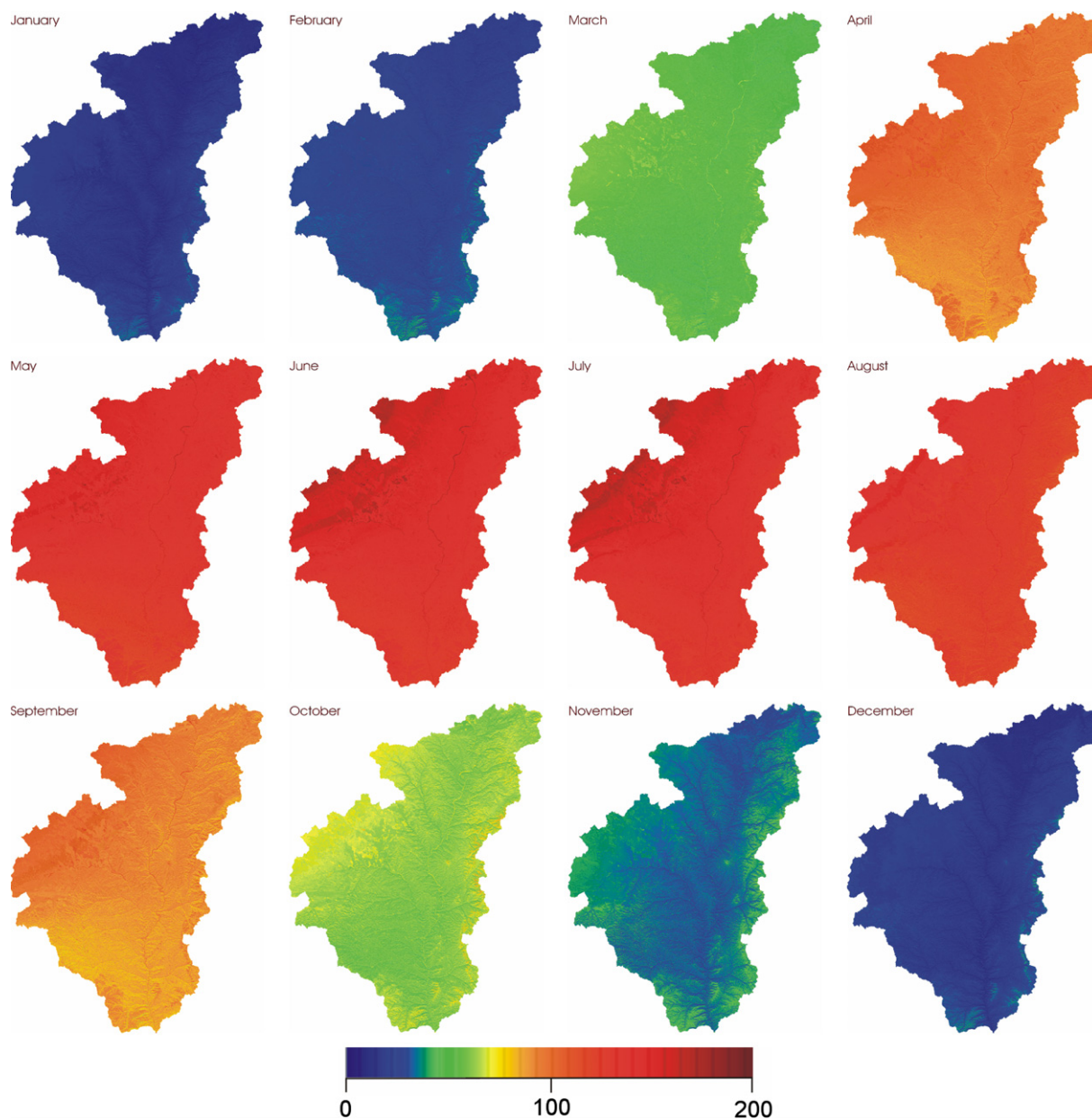
Figure 6 Monthly averages of ET_0 from the 21 years of data available, all units are mm month^{-1}.

secondary and tertiary models, using a QVPTPS with $m = 3$ and 4, respectively, were needed for some problematic months. Eight months had spurious data that were removed prior to fitting the remaining data with the primary spline model. Full results are presented in McVicar et al. (2005a).

Surfaces of monthly E_{pan} were generated for all 252 months (*i.e.*, from January 1980 through December 2000). Per grid-cell monthly averages of E_{pan} were calculated (see Fig. 8). The strong seasonal trend of $e_s - e_a$ and R_n are obvious. Values were typically in the order of 25—50 mm month^{-1} in the winter months, increasing to the maximum of about 300 mm month^{-1} in May, which gradually decreased over June to August (due to the influence of more cloud, hence lower n and R_n associated with the summer monsoons) and then quickly decreased during autumn (September to November).

Fig. 9 shows the monthly E_{pan} average, and measures of variance around this average associated with climate variability. These values were obtained by spatially averaging the resultant surfaces, and then temporally averaging those values.

For E_{pan}, $\sqrt{GCV(m, \lambda)}$/SD has a mean value of 0.53, the SD, maximum and minimum are 0.11, 0.82 and 0.26, respectively. The pessimistic relative error is 53% of the input data variance and, at worst, the pessimistic relative error is 82% of the input data variance. The mean value of $\sqrt{T(m, \lambda)}$/SD (a more optimistic expression of relative error) is 0.21, the SD, maximum and minimum are 0.06, 0.35 and 0.01, respectively. Given that 'true' relative error is somewhere between the pessimistic (53%) and optimistic (21%) expressions of relative error, we conclude that E_{pan} can be
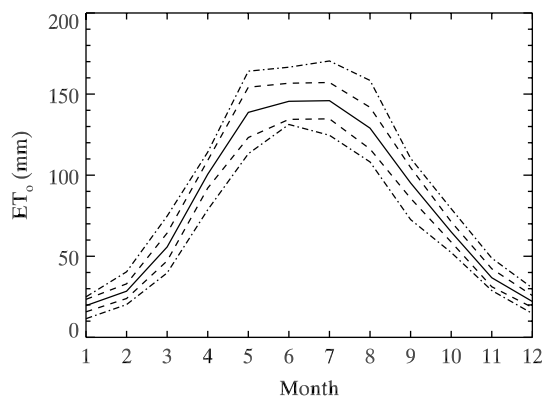
Figure 7 Time series of the surface-averaged monthly ET_0. The 21-year mean (solid line), ±1 standard deviation (dashed lines), and the minimum and maximum (dash–dot lines) are shown.

spatially interpolated without introducing more than moderate relative error.

Calculating K_{pan}

From the 252 K_{pan} surfaces, per grid-cell monthly averages shown in Fig. 10 illustrate a strong annual cycle with a range of about 0.21 K_{pan} units throughout the year. The minimum occurs in mid-spring (April) where values of approximately 0.44 were seen; this quickly increased through summer to reach a maximum of 0.65 in late summer (August), rapidly decreased in early autumn (September and October) and then gradually decreased through the winter months (November to March) to reach a minimum the following April. The general pattern is clearly seen in Fig. 11, where the effect of climate variability is seen by the introduced variance.

Only one other study has reported K_{pan} values using E_{pan} measurements based on 20-cm diameter Chinese micro-pans (Xu et al., 2006). For the upper reaches of the Yangtze River, a site relatively close to ours that experiences a somewhat similar climate, Xu et al. (2006) reported K_{pan}

values ranging from approximately 0.51 in winter to about 0.68 in summer; these values and their seasonality are very similar to our spatio-temporal averaged results (Fig. 11). To enable comparison of our results with K_{pan} values recorded with the pseudo-standard Class A pan, differences in E_{pan} measurements need to be discussed. As both are located above the ground (micro-pans sit 70 cm above and Class A pans 15 cm above, both on wooden frames), conduction of heat from the ground are assumed to be negligible (Oroud, 1998). For a micro-pan the ratio of surface area that heat (A_{heat}) from the environment can be transferred to the liquid water in the pan relative to the surface area that mass (*i.e.*, water — A_{water}) can be transferred to the environment is larger than for a Class A pan. A_{heat} is given by the water surface area plus the area of the sides of the pan (assuming no heat transfer through the bottom of the pan). Given the 20 cm diameter and 10 cm high walls of the Chinese micro-pans the ratio A_{heat}/A_{water} is 3.00, whereas for the 120.7 cm diameter by 25 cm high Class A pan this ratio is 1.83. Secondarily, the smaller volume of water in a Chinese micro-pan (20 cm diameter by 2 cm deep containing 628 g of water) may heat more rapidly than a Class A pan (120.7 cm diameter filled to 20 cm holds 228,841 g of water), slightly reducing the latent heat of vaporisation of water (Monteith and Unsworth, 1990). While relatively more water area would be shaded by the lip in the micro-pan compared to the Class A pan, especially at low solar zenith angles, over a month we expect that differences in the A_{heat}/A_{water} ratio and water temperature will outweigh differences in shading. While the energetics of a pan can be modelled (*e.g.*, Jacobs et al., 1998; Linacre, 1994; Molina Martínez et al., 2006; Rotstayn et al., 2006) this is outside the scope of this research. As the micro-pan is able to 'harvest' energy more efficiently from the environment (given its larger A_{heat}/A_{water} ratio) we assume that the rate of evaporation from a micro-pan would be larger than the rate of evaporation from a Class A pan — all other variables being equal. Calculating K_{pan} with a larger denominator means that the resulting expected (or typical) K_{pan} value will be smaller (for the micro-pan).

Ideal values of Class A K_{pan} values for given meteorological and site conditions can be derived from Allen et al.

Table 4 Statistical results when regressing measurements of E_{pan} as the independent variable with the dependent variable(s) shown

	Dependent variable(s)	r^2	RSD (mm month^{-1})	Constant (mm month^{-1})	Coefficient(s)
1	R_n	0.79	47.06	7.01	20.10
2	$e_s - e_a$	0.90	31.81	1.90	240.82
3	u	0.19	92.85	−7.31	83.61
4	$e_s - e_a$ and R_n	0.92	28.53	−5.72	181.87 6.10
5	$e_s - e_a$ and u	0.93	28.00	−49.25	228.80 29.79
6	$e_s - e_a$, u, and R_n	0.94	24.29	−56.36	170.53 29.54 6.04

The units of the dependent variables are MJ m^{-2} day^{-1} for R_n, kPa for $e_s - e_a$ and m s^{-1} for u. The units of values reported in the column with the heading 'coefficient(s)' are mm month^{-1} per the units of the appropriate dependent variable(s). The formula for the root squared difference (RSD) is provided in Eq. (4) and the constant and coefficient(s) are outputs from the linear regression modelling.
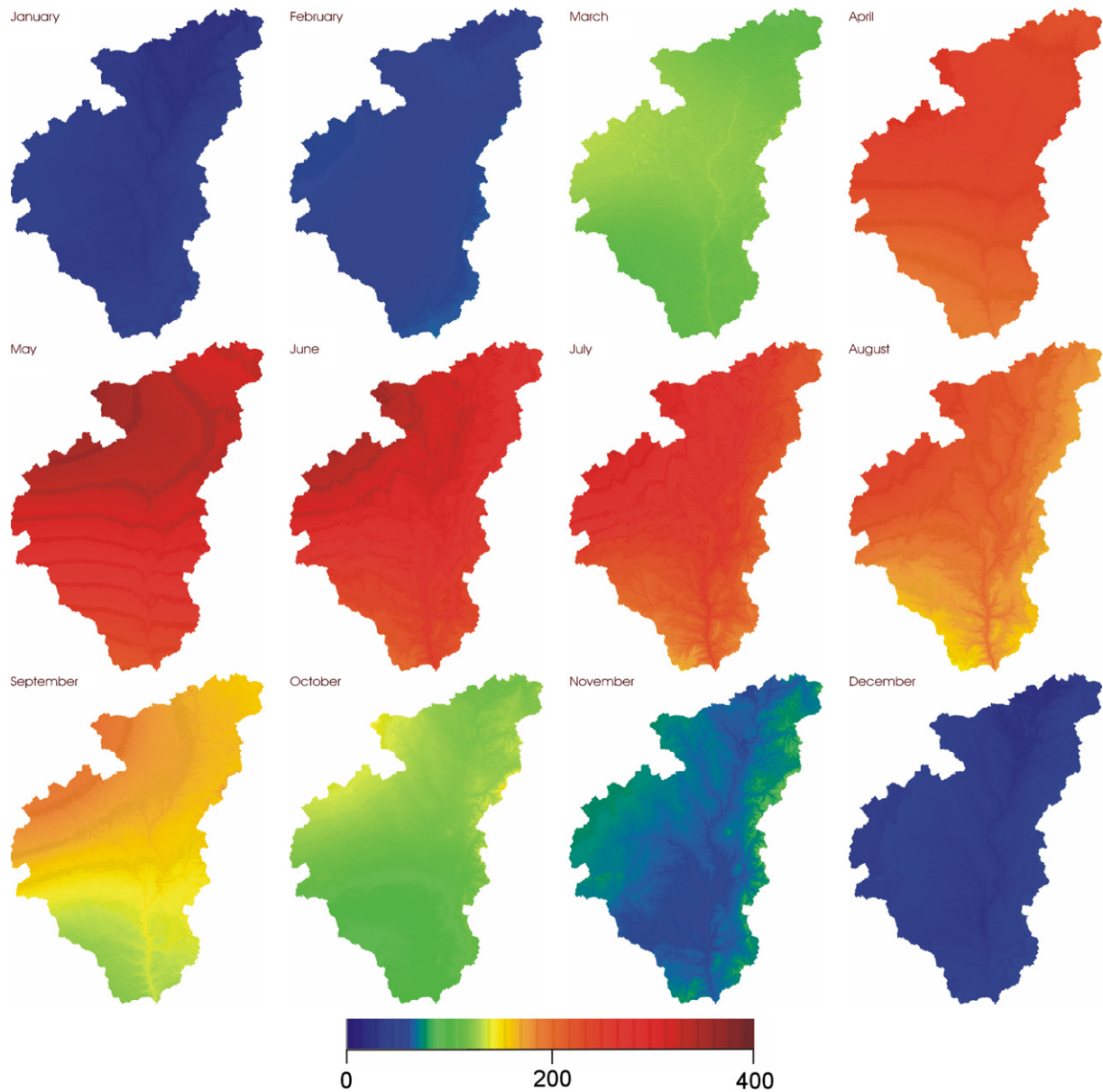
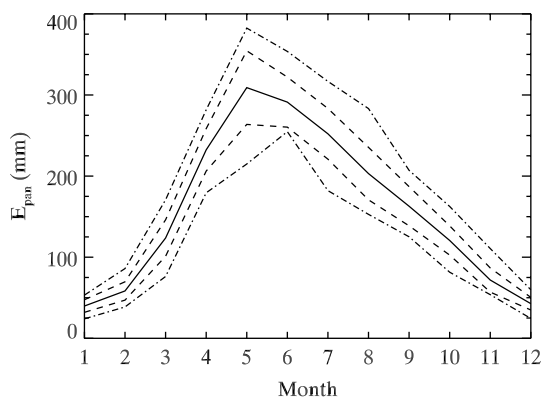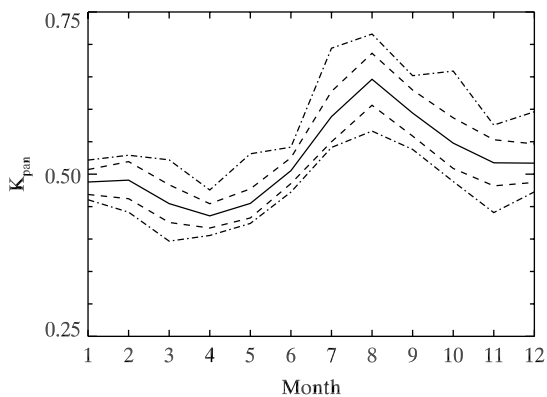**Figure 8** Monthly averages of E_{pan}, all units are mm month^{-1}.

Figure 9 Time series of surface-averaged monthly E_{pan}. The 21-year mean (solid line), ± 1 standard deviation (dashed lines), and the minimum and maximum (dash–dot lines) are shown.

(1998, pp. 81). Fig. 2c shows that monthly average u ranges from approximately 2.6 m s^{-1} in April to about 1.75 m s^{-1} in August, with Fig. 2g showing that monthly average relative humidity ranges from approximately 40% in April to just over 70% in August. Using Allen et al.'s (1998, pp. 81) definitions the April u can be considered 'moderate' and relative humidity 'low'; while for August u is 'light' and relative humidity 'high'. In April, using a Class A pan and assuming a 10 m fetch results in K_{pan} values of 0.60 for a green crop and 0.55 for a dry fallow soil. The corresponding values for August are 0.85 and 0.80. The ideal Class A pan K_{pan} values have a range of 0.3 K_{pan} units (from 0.85 to 0.55), and our micro-pan K_{pan} values for the 252 months have a range of 0.32 K_{pan} units (from 0.72 to 0.40 — see Fig. 11). For the two different pans, the ranges of K_{pan} values are similar, with the magnitude of the micro-pan K_{pan} values being smaller, as expected.
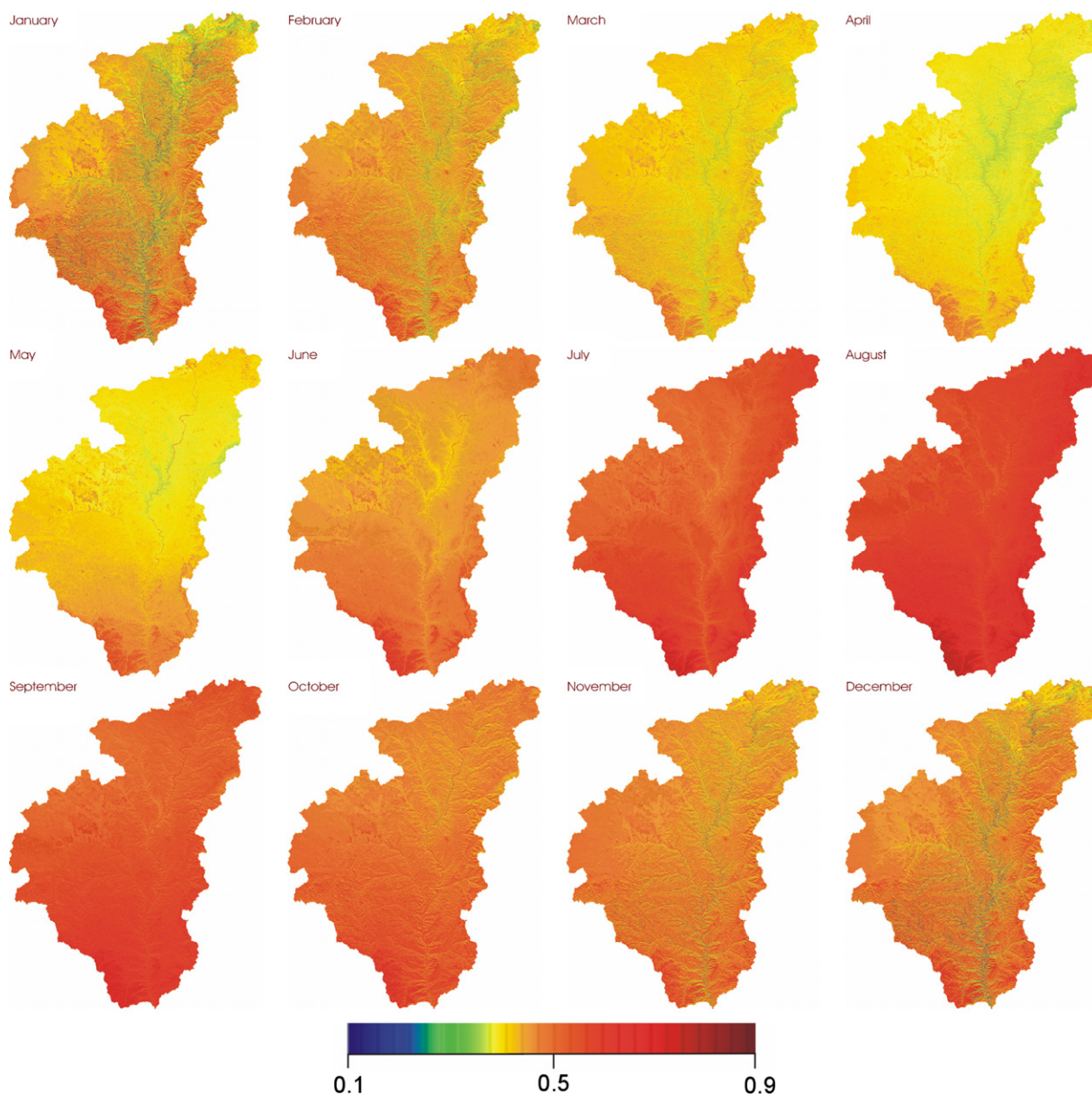
Figure 10   Monthly averages of K_{pan}. All values are a unitless ratio.

Figure 11   Time series of surface-averaged monthly K_{pan}. The 21-year mean (solid line), ±1 standard deviation (dashed lines), and the minimum and maximum (dash−dot lines) are shown.

Our micro-pan K_{pan} values (considering the impact of the smaller pan on E_{pan} and K_{pan} as discussed above) can be compared with Class A K_{pan} values reported in the international literature. For example, for a well-watered pasture in Florida, USA, Sumner and Jacobs (2005) report monthly K_{pan} values from 0.60 to 0.83, with Cohen et al. (2002) for Bet Dagan in Israel providing monthly mean K_{pan} values ranging from 0.70 to 0.84, occurring in February and October, respectively. Chiew et al. (1995, their Table 5) showed that seasonal averages of K_{pan} for 16 stations located across Australia ranged from 0.56 to 0.81. It is important to note that if K_{pan} values were spatially averaged across areas with fundamentally different climates then the range in the resultant values were dampened. Chiew et al. (1995) showed that when the values for all stations were spatially averaged, K_{pan} values were 0.68 in summer, 0.66 in autumn, 0.65 in winter, and 0.69 in spring. This dampening influence
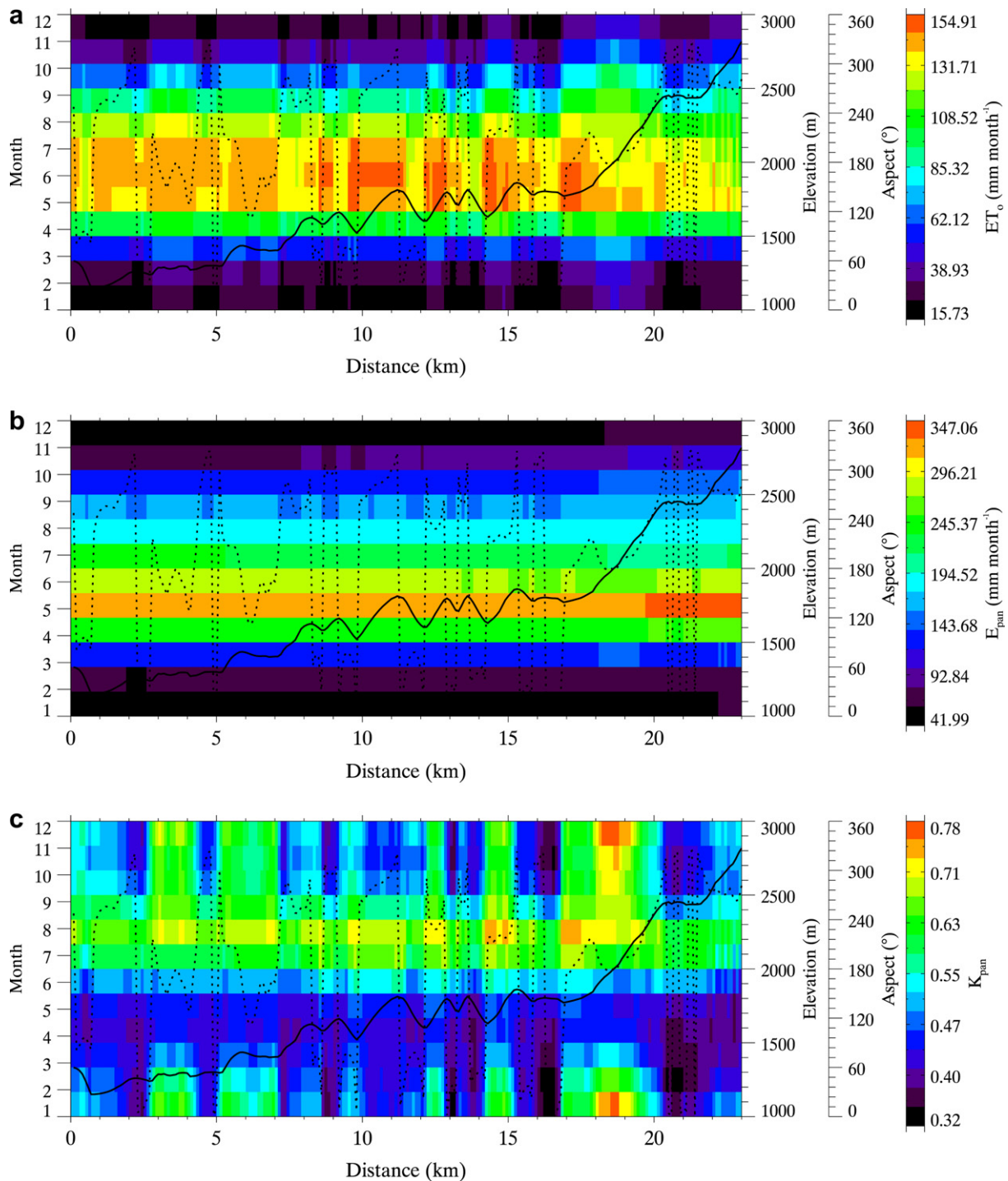
Figure 12 Monthly average values of: (a) ET_0; (b) E_{pan}; and (c) K_{pan} are shown for each 100 m grid cell along the 23 km long transect, located in Fig. 1. The elevation is shown by the solid line and aspect is represented by the dashed line, the transect runs from west (0 km) to east (23 km).

due to spatial averaging was confirmed by Chen et al. (2005) who reported seasonally averaged values that ranged only from 0.48 in spring to 0.59 in autumn using approximately 50 stations in the entire Yellow River basin. By way of contrast, Cohen et al.'s (2002) data summarised above was averaged only across time (not across space as the results presented by Chen et al., 2005 and Chiew et al., 1995 are) and has a larger range. These results suggest that distinct monthly variation of K_{pan} values were found when performing calculations at a single station, or when spatially averaging K_{pan} values in regions experiencing similar climatic conditions (as is the case of the CSHC), but not when spatially averaging from stations experiencing different climates.

To compliment previous results which encompass the entire study site, detailed spatio-temporal analysis was performed for ET_0, E_{pan} and K_{pan} at the 100 m grid-cell resolution for the 23 km transect introduced in Fig. 1. For the 252 monthly sequence for each grid-cell along the transect, the values of ET_0, E_{pan} and K_{pan} were extracted. Next, the mean monthly values for each 100 m resolution grid-cell were calculated, as shown in Fig. 12. The x-axis of this figure represents the distance along this transect and the primary (or left hand) y-axis are the months; topographic information is also shown on the secondary (or right hand) y-axes. In addition to a strong monthly signal for ET_0, Fig. 12a shows a response associated with rapidly varying aspects. This reveals the control that R_n has on the resulting values of ET_0 generated using an 'interpolate-then-calculate' (i.e., the result of spatial interpolation/modelling followed by per grid-cell calculations) approach. In contrast, less intra-monthly variation in E_{pan}, the direct output of spatial interpolation, is shown in Fig. 12b. Results for K_{pan} show a strong annual cycle modulated by the finer spatio-temporal variance introduced by ET_0, see Fig. 12c.

Detailed results for this 23-km long transect with elevations ranging from 1115 m to 2816 m reveal that monthly averages of K_{pan} are more strongly influenced by aspect than elevation, due to the surfaces of ET_0 being impacted by aspect. Comparisons with previous K_{pan} values measured using a micro-pan are similar in terms of magnitude and seasonality (Xu et al., 2006). Class A K_{pan} values that are both ideal (Allen et al., 1998) and measured (from Australia, Israel and southeast USA, respectively, Chiew et al., 1995; Cohen et al., 2002; Sumner and Jacobs, 2005) are slightly higher, as expected, with the annual ranges being similar.

Sensitivity analysis of ET_0, E_{pan} and K_{pan} to spatial interpolation

At the meteorological stations inside the study area values for ET_0, E_{pan} and K_{pan} were generated using data recorded at the stations or extracted from the resulting spatially modelled surfaces. From these the RSD, bias, relative RSD, and relative bias (see Eq. (4)) were calculated to assess the sensitivity of these variables to spatial interpolation/modelling; see Fig. 13.

Results for ET_0 are presented in Fig. 13a–d. For the RSD all values were less than 7.5 mm month^{-1}, though a strong seasonal pattern was seen, with values being larger in summer than winter (Fig. 13a). The mean bias of ET_0 was less than 1.0 mm month^{-1} for all months (Fig. 13b). For the hydrologically active portion of the year (March to October inclusive) the mean relative RSD was less than 7%, with the maximum relative RSD being in the order of 15%, see Fig. 13c. For winter — November to February — the mean and maximum relative RSD, and both the mean relative bias and extreme relative bias (Fig. 13d), all increased greatly. This was due to the small ET_{0_c} values in those months being used as the denominator to calculate the relative statistics, so even small actual differences (Fig. 13a and b) made large relative differences (Fig. 13c and d). While some individual winter months had large relative differences, this made little impact when considering regional water balance modelling given that both P and ET_0 were low in winter.

For E_{pan}, results for the four statistics are provided in Fig. 13e–h. The mean RSD was larger in summer (about 20 mm month^{-1}) with winter values approaching 0 mm month^{-1} (Fig. 13e). The mean bias was within the range of 3.5 mm month^{-1} for all months, see Fig. 13f. There was a slight seasonal trend in mean bias, with E_{pan_e} being larger than the measured E_{pan} values in winter (November to March; hence the bias is negative), and E_{pan_e} being smaller than the measured E_{pan} values during summer (April to October resulting in a positive bias). Fig. 13g shows the mean relative RSD ranges from just over 13% in winter (November and December) to approximately 7.5% in April, and for the hydrologically active portion of the year (March to October), the mean relative RSD was less than 10%. Fig. 13h shows that from March to October inclusive, the absolute mean relative bias was $\leqslant$ 2%, indicating that, on average, there was little difference in the E_{pan} results at the meteorological stations due to spatial interpolation. For winter — November to February — the increase in average absolute relative bias to $\leqslant$ 5% was a result of formulation of relative bias being greatly influenced by small differences when E_{pan} was low in winter. While the relative bias of individual months of E_{pan} varied from −32.5% to 18.5%, on average it was low, with values being in the range of ± 2% for most months.

Sensitivity analysis results for K_{pan} are shown in Fig. 13i–l. The RSD (Fig. 13i) exhibits a seasonal pattern, with mean values being smallest (approximately 0.02) in autumn (April and May) and increasing to 0.05 in winter (November to January). Fig. 13j shows that the mean bias for all months was close to zero. The average relative RSD (Fig. 13k) from February through October was less than 10%. From November to January this statistic degraded to large maximum values. A similar pattern was seen for the relative bias (Fig. 13l); it was within the range of 1% from March to November inclusive, while over winter (December to February) the statistics became worse. Winter was when the relative differences of ET_0 and E_{pan} were at their maximum, resulting in the larger relative differences of K_{pan}. The results demonstrated that for the hydrologically active part of the year — spring to autumn — small impacts arose from spatial interpolation/spatial modelling on the resultant K_{pan} values (with the mean relative RSD < 10%).

In summary, assessing the sensitivity of the three hydrological variables (generated in two ways at the 30 stations in the study site) provided increased confidence for using the resultant ET_0 or E_{pan} surfaces in regional hydrologic modelling. This was because their differences, and relative differences, were small in the hydrological active non-winter months. Differences in the absolute values for the three variables are provided in McVicar et al. (2005a).

Sensitivity analysis of R_n, ET_0, and K_{pan} to land surface parameterisation

The bias and relative bias (Eq. (5)) were calculated for R_n, ET_0, and K_{pan} by using land-cover dependent temporally varying land surface parameters in SRAD (see Tables 1 and 2), or by using static estimates of LAI and α in SRAD. For R_n the average bias for the entire CSHC reaches its maximum value of 0.02 MJ m^{-2} day^{-1} in August with the minimum of −0.39 MJ m^{-2} day^{-1} occurring in April, see Fig. 14a. A
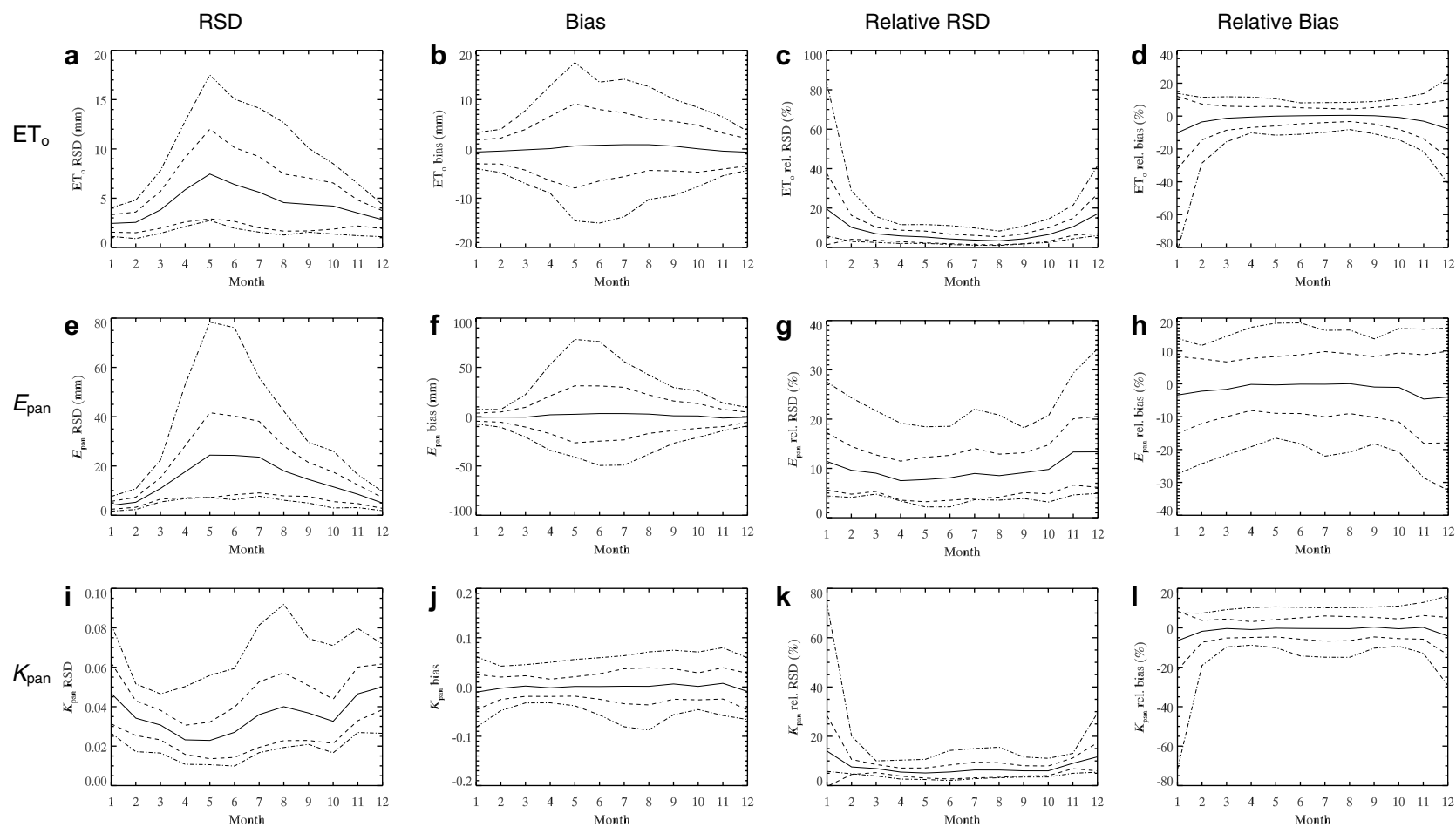
Figure 13 Monthly figures of: (a) ET$_0$ RSD; (b) ET$_0$ bias; (c) ET$_0$ relative RSD; (d) ET$_0$ relative bias. With (e) to (h) are for E_{pan}, and (i) to (l) are for K_{pan}, and for both cases the statistics reported in the 4 plots are the same order as for ET$_0$ provided in (a)−(d). The 21-year mean (solid line), ±1 standard deviation (dashed lines), and the minimum and maximum (dash−dot lines) are shown.
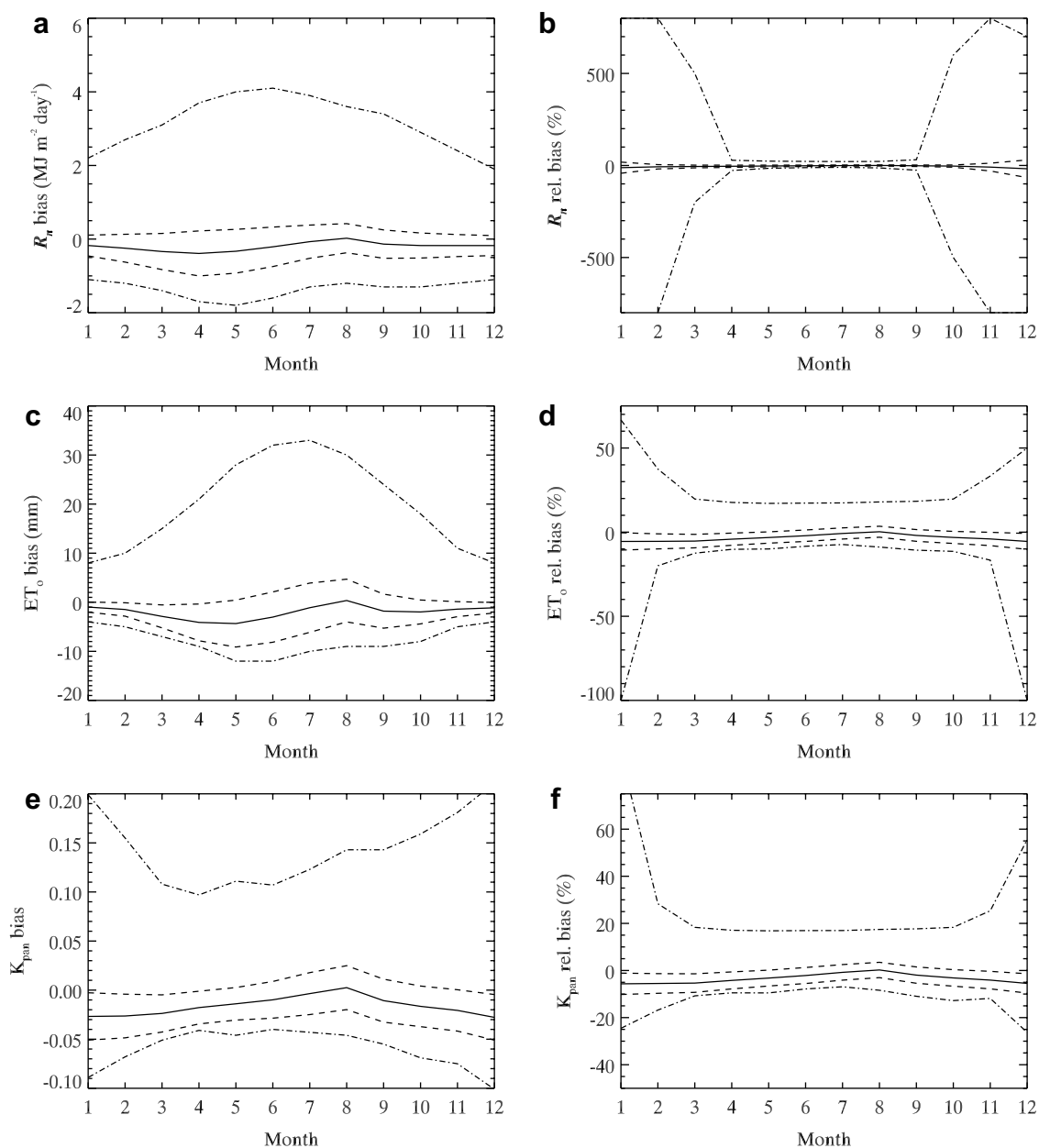
Figure 14 Monthly bias and relative bias of R_n (a and b, respectively); ET_0 (c and d, respectively) and K_{pan} (e and f, respectively) to changes in land surface parameterisation of LAI and α used in SRAD. The 21-year mean (solid line), ±1 standard deviation (dashed lines), and the minimum and maximum (dash−dot lines) are shown.

positive bias is primarily due to the dynamic α being set to 0.14 for forest (Table 2) in some months causing R_{s_out} to reduce, so R_n increases (when compared to the static case when $\alpha = 0.23$). The negative bias is mainly caused by the dynamic α being >0.23 for most of the year for the agriculture, pasture and desert land-cover classes (Table 2), resulting in an increase of R_{s_out} and hence a decrease of R_n (compared to when $\alpha = 0.23$). As these land-covers dominate the CSHC (Li et al., 2005b; McVicar et al., 2005a) the time series of the area-averaged bias is inverted relative to the prescribed α time series of these classes (Table 2). At a grid-cell basis the largest bias was 4.1 MJ m^{-2} day^{-1} recorded in June, and the smallest was −1.8 MJ m^{-2} day^{-1} in May. The average relative bias (Fig. 14b) ranges from 0.12% in August to

−17.83% in December, with per grid-cell relative biases ranging from 31.25% (September) to −27.27% (April) in the hydrologically active portion of the year (April to September), and becoming greater than 200% on a per grid-cell basis in winter. This large relative bias is due to the value of the denominator used to calculate the relative statistics approaching 0.0 MJ m^{-2} day^{-1}, hence small actual differences seem relatively large.

For ET_0 the study area averaged bias ranges from 0.35 mm month^{-1} in August to −4.35 mm month^{-1} in May. On a per grid-cell basis the maximum bias (33 mm month^{-1}) occurs in August, and the minimum (−12 mm month^{-1}) in both May and June, see Fig. 14c. A positive bias is associated with the forest and sparse forest classes, as the relative

increase in R_n associated with $\alpha < 0.23$ results in ET_0 increasing (compared to the static case when $\alpha = 0.23$). The negative bias is caused by the decrease in R_n for the dynamic case for agriculture, pasture and desert land-cover classes ($\alpha > 0.23$ for most months) compared to the static case. As these land-cover classes occupy most of CSHC this results in the monthly trend of the area averaged bias (Fig. 14c.) essentially being inverted from the prescribed α used in the dynamic SRAD modelling. The area averaged relative bias of ET_0 due to having dynamic or static land surface parameterisations of SRAD is less than 5% for April to November inclusively (Fig. 14d). On a per grid-cell basis the range of the relative bias increases dramatically in winter, again due to the small values of the denominator used in the expression.

For K_{pan} the area-average bias ranges from -0.03 in winter (December to February) to 0.0 in summer (July and August), see Fig. 14e, with the temporal trend following the α based land-cover class argument as presented above. In summer the area weighted difference of dynamic and static α are minimal, causing this result. Both extreme per-pixel biases occur in December, ranging from 0.21 to -0.10. The mean relative bias is less than 5% from April to November, inclusive — see Fig. 14f. The smallest is -5.6 % in January and the largest value of 0.22% occurs in August when the dynamically prescribed α is set to 0.23 for both the agricultural and pasture land-cover classes (Table 2) which equals the static α used in this sensitivity analysis, resulting in the minimal relative bias for this month.

The findings from this sensitivity analysis illustrate that utilising a temporally dynamic and land-cover dependent parameterisation of LAI and α in SRAD impacts the area averaged relative bias by less than 5% for R_n, ET_0, and K_{pan} for the hydrologically active portion of the year, defined as April to October inclusively. This provided increased confidence for using the resultant surfaces in regional hydrologic modelling.

Conclusions

For the first time, high resolution surfaces of ET_0 have been developed regionally considering the influence of topography on the forcing meteorological data. This was achieved by spatially interpolating the required meteorological variables (taking elevation into account) and spatially modelling the radiation environment (considering topography) to 100 m resolution data prior to calculating ET_0 at each grid-cell. This approach is called 'interpolate-then-calculate', and it maintains topographic influences on the forcing data — especially net radiation. Implementing an 'interpolate-then-calculate' approach to spatially distribute ET_0 in the CSHC uses information from >11 million points (primarily the 58 stations and secondarily the >11 million grid-cells in the DEM), whereas in contrast, using a geometric two dimensional 'calculate-then-interpolate' approach would have only used information from the 58 points in, and around, the CSHC. Since many communities across the globe rely on water resources derived from topographically complex upper-catchments, the value of this approach for spatially distributing ET_0 is widespread.

In addition to the larger issue-based conclusions drawn above, other conclusions specific to our data analysis can be made. They are:

(1) T_{max}, T_{min}, u and e_a were best interpolated using a TVPTPS using elevation as a covariate;

(2) n was optimally interpolated with a TVPTPS using the monthly air temperature range as a covariate;

(3) unexpectedly P was best modelled with a BVTPS;

(4) T_{max} was interpolated with low relative error, both T_{min} and e_a had moderate relative error, and u, n and P had relatively higher errors;

(5) average monthly variations of lapse rates were steeper in summer than winter and those for T_{max} were steeper than those for T_{min};

(6) monthly climatologies of the NSED for u and e_a also showed strong seasonal values, and this was the first time that monthly climatologies of NSED for both u and e_a have been determined;

(7) R_n was modelled accounting for topographic factors and temporally dynamic land-cover based estimates of LAI and α to provide physically realistic estimates;

(8) spatial and temporal patterns of the 252-month sequence of output ET_0 surfaces were biophysically reasonable, with average values ranging from approximately 20 mm month^{-1} in winter (January and December) to about 150 mm month^{-1} in summer (May to July);

(9) monthly surfaces of E_{pan} were generated using a quint-variate partial thin plate spline which incorporated a BVTPS function of longitude, latitude with a constant linear dependences on $e_s - e_a$, u, and R_n;

(10) the spatial and temporal patterns of E_{pan} were physically sensible; average values ranged from about 40 mm month^{-1} in winter (January and December) to over 300 mm month^{-1} in May;

(11) spatially then temporally average values of the pan coefficient ($K_{pan} = ET_0/E_{pan}$) varied from the minimum of 0.44 in April, increasing to a maximum of 0.65 in late summer (August) before decreasing in autumn and winter;

(12) the range and seasonality of K_{pan} values agreed well with the only other study reporting values made using E_{pan} measurements from a micro-pan. As micro-pans have a higher ratio of surface area for heat transfer to surface area for mass transfer, we assumed this difference primarily controls micro-pans having higher rates of evaporation relative to the larger Class A pans experiencing the same meteorological conditions. This explained why our K_{pan} values were slightly lower than both ideal and measured values reported in the international literature when Class A pans were used;

(13) grid-cell analysis of a transect with over 1650 m elevation range revealed that aspect influenced the resultant ET_0 calculations to a greater extent than elevation, while the impact of aspect was less pronounced for E_{pan}. This was due to E_{pan} being spatially interpolated from isolated measurements (akin to using a 'calculate-then-interpolate' approach) compared to the ET_0 surfaces that were generated using an 'interpolate-then-calculate' approach;

(14) sensitivity analysis for ET_0, E_{pan} and K_{pan} performed at the 30 stations located in the study site found that the average relative RSD was less than 10% and the absolute relative bias was smaller than 1.5% from March to November, inclusive. These results indicated that the spatial modelling introduced negligible differences at the stations during the hydrologically active portion of the year; and

(15) sensitivity analysis of R_n, ET_0, and K_{pan} to the parameterisation of LAI and α in SRAD showed that the area averaged relative bias was less than 5% during the hydrologically active portion of the year.

Finally, the methods developed here can be utilised to realistically spatially distribute ET_0, E_{pan} and K_{pan} for other topographically complex terrestrial regions. The resulting spatially-distributed time-series of hydrometerological data can be used for many applications including simulating the hydrological response of current and planned re-vegetation activities implemented as part of the ''Grain for Green'' project (McVicar et al., in press; Zhang et al., in press), and mapping perennial vegetation suitability (McVicar et al., 2005b) used in those programs.

Acknowledgements

References

Allen, R.G., Pereira, L.S., Raes, D., Smith, M., 1998. Crop evapotranspiration — Guidelines for computing crop water requirements. FAO Irrigation and Drainage Paper 56, Rome, Italy.

Barry, R.G., 1992. Mountain Weather and Climate, second ed. Routledge, London.

Beniston, M., Rebetez, M., 1996. Regional behavior of minimum temperatures in Switzerland for the period 1979—1993. Theoretical and Applied Climatology 53, 231—244.

Bergeron, T., 1960. Preliminary results of project pluvius. In: Commission of Land Erosion General Assembly, (IASH), pp. 226—237.

Bolstad, P.V., Swift, L., Collins, F., Régnière, J., 1998. Measured and predicted air temperatures at basin to regional scales in the southern Appalachian mountains. Agricultural and Forest Meteorology 91, 161—176.

Briggs, P.R., Cogley, J.G., 1996. Topographic bias in mesoscale precipitation networks. Journal of Climate 9, 205—218.

Bristow, K.L., Campbell, G.S., 1984. On the relationship between incoming solar radiation and daily maximum and minimum temperature. Agricultural and Forest Meteorology 31, 159—166.

Brutsaert, W.H., 1982. Evaporation into the Atmosphere Theory, History and Applications. Kluwer Academic Publishers, Dordrecht.

Chen, J., He, D., Cui, S., 2003. The response of river water quality and quantity to the development of irrigated agriculture in the last 4 decades in the Yellow River basin, China. Water Resources Research 39, 1047. doi:10.1029/2001WR00123.

Chen, R., Ersi, K., Yang, J., Lu, S., Zhao, W., 2004. Validation of five global radiation models with measured daily data in China. Energy Conversion and Management 45, 1759—1769.

Chen, D.L., Gao, G., Xu, C.-Y., Guo, J., Ren, G.Y., 2005. Comparison of the Thornthwaite method and pan data with the standard Penman-Monteith estimates of reference evapotranspiration in China. Climate Research 28, 123—132.

Chiew, F.H.S., McMahon, T.A., 1992. An Australian comparison of Penman's potential evapotranspiration and Class A evaporation pan data. Australian Journal of Soil Research 30, 101—112.

Chiew, F.H.S., Kamaladasa, N.N., Malano, H.M., McMahon, T.A., 1995. Penman—Monteith, FAO-24 reference crop evapotranspiration and Class-A pan data in Australia. Agricultural Water Management 28, 9—21.

Chuanyan, Z., Zhongren, N., Zhaodong, F., 2004. GIS-assisted spatially distributed modeling of the potential evapotranspiration in semi-arid climate of the Chinese Loess Plateau. Journal of Arid Environments 58, 387—403.

Cohen, S., Ianetz, A., Stanhill, G., 2002. Evaporative climate changes at Bet Dagan, Israel, 1964—1998. Agricultural and Forest Meteorology 111, 83—91.

Daly, C., 2006. Guidelines for assessing the suitability of spatial climate data sets. International Journal of Climatology 26, 707—721.

Davis, B.M., 1987. Uses and abuses of cross-validation in geostatistics. Mathematical Geology 19, 241—248.

Dodd, A.V., 1965. Dew point distribution in the contiguous United States. Monthly Weather Review 93, 113—121.

Donohue, R.J., Roderick, M.L., McVicar, T.R., 2007. On the importance of including vegetation dynamics in Budyko's hydrological model. Hydrology and Earth System Sciences 11, 983—995.

Doorenbos, J., Pruitt, W.O., 1975. Guidelines for Predicting Crop Water Requirements. FAO Irrigation and Drainage Paper No. 24, Rome, pp. 193.

Doorenbos, J., Pruitt, W.O., 1977. Guidelines for Predicting Crop Water Requirements. FAO Irrigation and Drainage Paper No. 24— Revised Edition, Rome. pp. 156.

Garcia, M., Raes, D., Allen, R., Herbas, C., 2004. Dynamics of reference evapotranspiration in the Bolivian highlands (Altiplano). Agricultural and Forest Meteorology 125, 67—82.

Geiger, R., 1950. The Climate Near the Ground, second ed. Harvard University Press, Cambridge.

Giorgi, F., Hurrell, J.W., Marinucci, M.R., Beniston, M., 1997. Elevation dependency of the surface climate change signal: a model study. Journal of Climate 10, 288—296.

Gong, L., Xu, C., Chen, D., Halldin, S., Chen, Y.D., 2006. Sensitivity of the Penman—Monteith reference evapotranspiration to key climatic variables in the Changjiang (Yangtze River) basin. Journal of Hydrology 329, 620—629.

Granger, R.J., 1989. An examination of the concept of potential evaporation. Journal of Hydrology 111, 9—19.

Gustavsson, T., Karlsson, M., Bogren, J., Lindqvist, S., 1998. Development of temperature patterns during clear nights. Journal of Applied Meteorology 37, 559—571.

Hargreaves, G.H., Samni, Z.A., 1985. Reference crop evapotranspiration from temperature. Applied Engineering in Agriculture 1, 96—99.

Hong, Y., Nix, H.A., Hutchinson, M.F., Booth, T.H., 2005. Spatial interpolation of monthly mean climate data for China. International Journal of Climatology 25, 1369—1379.

Huang, B.W., 1988. River conservancy and agricultural development on the North China Plains and Loess Highlands: strategies and research. Great Plains Quarterly 6, 218—224.

Hungerford, R.D., Nemani, R.R., Running, S.W., Coughlin, J.C., 1989. MTCLIM: A Mountain Microclimate Simulation Model. USDA Forest Service, INT-414.

Huntington, T.G., 2006. Evidence for intensification of the global water cycle: review and synthesis. Journal of Hydrology 319, 83—95.

Hutchinson, M.F., 1989. A new objective method for spatial interpolation of meteorological variables from irregular networks applied to the estimation of monthly mean solar radiation, temperature, precipitation and windrun. CSIRO Division of Water Resources, Technical Memoranda, 89/5.

Hutchinson, M.F., 1991. The application of thin plate partial smoothing splines to continent-wide data assimilation. In: Jasper, J.D., (Ed.), Data Assimilation Systems, BMRC Research Report No. 27. Bureau of Meteorology, Melbourne, Australia. pp. 104—113.

Hutchinson, M.F., 1995. Interpolating mean rainfall using thin plate smoothing splines. International Journal of Geographical Information Science 9, 385—403.

Hutchinson, M.F., 1998. Interpolation of rainfall data with thin plate smoothing splines: I two dimensional smoothing of data with short range correlation. Journal of Geographic Information and Decision Analysis 2, 152—167.

Hutchinson, M.F., 2004a. ANUDEM Version 5.1 User Guide. The Australian National University, Centre for Resource and Environmental Studies, Canberra, http://cres.anu.edu.au/outputs/software.php.

Hutchinson, M.F., 2004b. ANUSPLIN Version 4.3 User Guide. The Australian National University, Centre for Resource and Environmental Studies, Canberra, http://cres.anu.edu.au/outputs/software.php.

Hutchinson, M.F., Gessler, P.E., 1994. Splines — more than just a smooth interpolator. Geoderma 62, 45—67.

Hutchinson, M.F., Booth, T.H., Nix, H.A., McMahon, J.P., 1984a. Estimating monthly mean values of daily total solar radiation for Australia. Solar Energy 32, 277—290.

Hutchinson, M.F., Kalma, J.D., Johnson, M.E., 1984b. Monthly estimates of wind speed and wind run for Australia. Journal of Climatology 4, 311—324.

Jacobs, A.F.G., Heusinkveld, B.G., Lucassen, D.C., 1998. Temperature variation in a class A evaporation pan. Journal of Hydrology 206, 75—83.

Jeffrey, S.J., Carter, J.O., Moodie, K.B., Beswick, A.R., 2001. Using spatial interpolation to construct a comprehensive archive of Australian climate data. Environmental Modelling and Software 16, 309—330.

Ke, B.S., Zhou, S.Y., 2005. Land acquisition in China: policy development and reform recommendations. In: Sonntag, B.H., Huang, J.K, Rozelle, S., and Skerritt, J.H., (Eds.), China's Agricultural and Rural Development in the Early 21st Century: Challenges, Opportunities and Policy Options. ACIAR Monograph No. 116: Canberra, pp. 469—487.

Keig, G., McApine, J.R., 1974. WATBAL: A computer system for estimation and analysis of soil moisture regimes from simple climatic data. CSIRO Division of Land Use Research, Canberra.

Kossmann, M., Vögtlin, R., Corsmeier, U., Vogel, B., Fiedler, F., Binder, H.J., Kalthoff, N., Beyrich, F., 1998. Aspects of the convective boundary layer structure over complex terrain. Atmospheric Environment 32, 1323—1348.

Lam, N.S., 1983. Spatial interpolation methods: a review. The American Cartographer 10, 129—149.

Laslett, G.M., 1994. Kriging and splines: an empirical comparison of their predictive performance in some applications. Journal of the American Statistical Association 89, 391—409.

Lhomme, J.-P., 1997. Towards a rational definition of potential evaporation. Hydrology and Earth System Sciences 1, 257—264.

Li, GY., 2003. Ponderation and Practice of the Yellow River Control. Yellow River Conservancy Press, Zhengzhou.

Liang, Y.M., Li, R., Cheng, J.M., Liu, G.B., Chen, Y.M., Liu, W.Z., 2003. Vegetation Construction on the Loess Plateau. Yellow River Conservancy Press, Zhengzhou, in Chinese and English.

Li, S.G., Harazono, Y., Oikawa, T., Zhao, H.L., He, Z.Y., Chang, X.L., 2000. Grassland desertification by grazing and the resulting micrometeorological changes in Inner Mongolia. Agricultural and Forest Meteorology 102, 125—137.

Li, S.G., Harazono, Y., Zhao, H.L., He, Z.Y., Chang, X.L., Zhao, X.Y., Zhang, T.H., Oikawa, T., 2002. Micrometeorological changes following establishment of artificially established artemisia vegetation on desertified sandy land in the Horqin sandy land, China and their implication on regional environmental change. Journal of Arid Environments 52, 101—119.

Li, L.T., McVicar, T.R., Van Niel, T.G., Mu, X.M., Zhang, X.P., Yang, Q.K., Liu, Z.H., 2005a. Quality control of 21 years of monthly meteorological and hydrological data in the Coarse Sandy Hilly Catchments of the Loess Plateau, China. CSIRO Land and Water Technical Report 6/05, Canberra, Australia, http://www.clw.csiro.au/publications/technical2005/tr6-05.pdf.

Li, L.T., McVicar, T.R., Van Niel, T.G., Zhang, L., Li, R., Yang, Q.K., Zhang, X.P., Mu, X.M., Wen, Z.M., Liu, W.Z., Zhao, Y.A., Liu, Z.H., 2005b. A bilingual user's guide for the decision support tool for managing re-vegetation and its impact on hydrology (ReVegIH) in the Coarse Sandy Hilly Catchments of the Loess Plateau, China. CSIRO Land and Water Technical Report 19/05, Canberra, http://www.clw.csiro.au/publications/technical2005/tr19-05.pdf.

Linacre, ET., 1994. Estimating U.S. Class—A pan evaporation from few climate data. Water International 19, 5—14.

Lin, W., Lu, E., 1998. Correlations between monthly average global solar radiation on horizontal surfaces and relative duration of sunshine in Yunnan Province, China. Renewable Energy 13, 355—362.

Liu, B.H., Xu, M., Henderson, M., Qi, Y., Li, Y.Q., 2004. Taking China's temperature: daily range, warming trends, and regional variations, 1955—2000. Journal of Climate 17, 4453—4462.

Lookingbill, T.R., Urban, D.L., 2003. Spatial estimation of air temperature differences for landscape-scale studies in montane environments. Agricultural and Forest Meteorology 114, 141—151.

Martinez-Lonano, J.A., Tena, F., Onrubia, J.E., Rubia, J., 1984. The historical evolution of the Ångström formula and its modifications: review and bibliography. Agricultural and Forest Meteorology 33, 109—128.

McKenney, M.S., Rosenberg, N.J., 1993. Sensitivity of some potential evapotranspiration estimation methods to climate change. Agricultural and Forest Meteorology 64, 81—110.

McKenney, D.W., Mackey, B.G., Zavitz, B.L., 1999. Calibration and sensitivity analysis of a spatially-distributed solar radiation

model. International Journal of Geographical Information Science 13, 49—65.

McVicar, T.R., Jupp, D.L.B., 1999. Estimating one-time-of-day meteorological data from standard daily data as inputs to thermal remote sensing based energy balance models. Agricultural and Forest Meteorology 96, 219—238.

McVicar, T.R., Jupp, D.L.B., 2002. Using covariates to spatially interpolate moisture availability in the Murray-Darling basin: a novel use of remotely sensed data. Remote Sensing of Environment 79, 199—212.

McVicar, T.R., Zhang, G., Bradford, A.S., Wang, H., Dawes, W.R., Zhang, L., Lingtao, L., 2002. Monitoring regional agricultural water use efficiency for Hebei Province on the North China Plain. Australian Journal of Agricultural Research 53, 55—76.

McVicar, T.R., Li, L.T., Van Niel, T.G., Hutchinson, M.F., Mu, X.M., Liu, Z.H., 2005a. Spatially distributing 21 years of monthly hydrometeorological data in China: spatio-temporal analysis of FAO-56 crop reference evapotranspiration and pan evaporation in the context of climate change. CSIRO Land and Water Technical Report, 8/05, Canberra, Australia, http://www.clw.csiro.au/publications/technical2005/tr8-05.pdf.

McVicar, T.R., Wen, Z.M., Van Niel, T.G., Li, L.T., Yang, Q.K., Li, R., Jiao, F., 2005b. Mapping perennial vegetation suitability and identifying target and priority areas for implementing the re-vegetation program in the Coarse Sandy Hilly Catchments of the Loess Plateau, China. CSIRO Land and Water Technical Report, 18/05, Canberra, Australia, http://www.clw.csiro.au/publications/technical2005/tr18-05.pdf.

McVicar, T.R., Li, L.T., Van Niel, T.G., Zhang, L., Li, R., Yang, Q.K., Zhang, X.P., Mu, X.M., Wen, Z.M., Liu, W.Z., Zhao, Y.A., Liu, Z.H., Gao, P., in press. Developing a decision support tool for China's re-vegetation program: simulating regional impacts of afforestation on average annual streamflow in the Loess Plateau. Forest Ecology and Management.

Meza, F., Varas, E., 2000. Estimation of mean monthly solar global radiation as a function of temperature. Agricultural and Forest Meteorology 100, 231—241.

Miller, C.A., Davenport, A.G., 1998. Guidelines for the calculation of wind speed-ups in complex terrain. Journal of Wind Engineering and Industrial Aerodynamics, 189—197.

Mo, X., Liu, S., Lin, Z., Zhao, W., 2004. Simulating temporal and spatial variation of evapotranspiration over the Lushi basin. Journal of Hydrology 285, 125—142.

Molina Martínez, J.M., Martínez Alvarez, V., González-Real, M.M., Baille, A., 2006. A simulation model for predicting hourly pan evaporation from meteorological data. Journal of Hydrology 318, 250—261.

Monteith, J.L., 1965. Evaporation and environment. In: Fogg, G.E. (Ed.), State and Movement of Water in Living Organisms, 19th Symposium Society for Experimental Biology. Cambridge University Press, pp. 205—234.

Monteith, J.L., Unsworth, M.H., 1990. Principles of Environmental Physics. Edward Arnold, London.

Moore, I.D., Norton, T.W., Williams, J.E., 1993. Modelling environmental heterogeneity in forested landscapes. Journal of Hydrology 150, 717—747.

Nalder, I.A., Wein, R.W., 1998. Spatial interpolation of climatic normals: test of a new method in the Canadian boreal forest. Agricultural and Forest Meteorology 92, 211—225.

Oroud, I.M., 1998. The influence of heat conduction on evaporation from sunken pans in hot, dry environment. Journal of Hydrology 210, 1—10.

Oudin, L., Hervieu, F., Michel, C., Perrin, C., Andréassian, V., Anctil, F., Loumagne, C., 2005. Which potential evapotranspiration input for a lumped rainfall-runoff model? Part 2-Towards a simple and efficient potential evapotranspiration model for rainfall—runoff modelling. Journal of Hydrology 303, 290—306.

Penman, H.L., 1948. Natural evaporation from open water, bare soil and grass. Proceedings of the Royal Society, London A 193, 120—145.

Penman, H.L., 1956. Evaporation: an introductory survey. Netherlands Journal of Agricultural Science 4, 9—29.

Pepin, N.C., 2000. Twentieth century change in the climate record for the Front Range, Colorado, U.S.A. Arctic, Antarctic and Alpine Research 32, 135—146.

Pepin, N.C., Losleben, M., 2002. Climate change in the Colorado Rocky Mountains: free air versus surface temperature trends. International Journal of Climatology 22, 311—329.

Prata, A.J., 1996. A new long-wave formula for estimating downward clear-sky radiation at the surface. Quarterly Journal of the Royal Meteorological Society 122, 1127—1151.

Prescott, J.A., 1940. Evaporation from water surface in relation to solar radiation. Transactions of the Royal Society of South Australia 64, 114—125.

Price, D.T., McKenny, D.W., Nalder, I.A., Hutchinson, M.F., Kesteven, J.L., 2000. A comparison of two statistical methods for spatial interpolation of Canadian monthly mean climate data. Agricultural and Forest Meteorology 101, 81—94.

Priestley, C.H.B., Taylor, R.J., 1972. On the assessment of surface heat flux and evaporation using large-scale parameters. Monthly Weather Review 100, 81—92.

Qiang, Z., Ronghui, H., 2004. Parameters of land-surface processes for Gobi in North-West China. Boundary-Layer Meteorology 110, 471—478.

Raupach, M.R., Finnigan, J.J., 1997. The influence of topography on meteorological variables and surface-atmosphere interactions. Journal of Hydrology 190, 182—213.

Ren, M.E., Yang, R.Z., Bao, H.S., 1985. An Outline of China's Physical Geography. Foreign Language Press, Beijing.

Roderick, M.L., 2006. The ever-flickering light. Trends in Ecology & Evolution 21, 3—5.

Roderick, M.L., Farquhar, G.D., 2005. An analysis of pan evaporation changes in relation to possible explanatory factors. In: Gifford, R.M. (Ed.), Pan Evaporation: an Example of the Detection and Attribution of Trends in Climate Variables. Shine Dome, Australian Academy of Science, Canberra, Australia. Australian Academy of Science, National Committee for Earth System Science, pp. 79—81.

Roe, G.H., 2005. Orographic precipitation. Annual Review of Earth and Planetary Sciences 33, 645—671.

Rolland, C., 2003. Spatial and seasonal variations of air temperature lapse rates in Alpine regions. Journal of Climate 16, 1032—1046.

Rotstayn, L.D., Roderick, M.L., Farquhar, G.D., 2006. A simple pan-evaporation model for analysis of climate simulations: evaluation over Australia. Geophysical Research Letters 33, L17715. doi:10.1029/2006GL02711.

Running, S.W., Nemani, R., Hungerford, R.D., 1987. Extrapolation of synoptic meteorological data in mountainous terrain and its uses for simulating forest evapotranspiration and photosynthesis. Canadian Journal of Forest Research 17, 472—483.

Sharples, J.J., Hutchinison, M.F., Kesteven, J.L., submitted for publication. Spatio-temporal trends in pan evaporation across Australia. International Journal of Climatology.

Shen, H.Q., 1991. China Loess Plateau 1:500 000 land-use map, part of the Loess Plateau Resources and Environmental Remote Sensing Series, In: Xi'an Atlas Press, Xi'an.

Shen, D.J., Varis, O., 2001. Climate change in China. AMBIO: A Journal of the Human Environment 30, 381—383.

Shenbin, C., Yunfeng, L., Thomas, A., 2006. Climatic change on the Tibetan Plateau: potential evapotranspiration trends from 1961-2000. Climatic Change 76, 291—319.

Shi, H., Shao, M., 2000. Soil and water loss from the Loess Plateau in China. Journal of Arid Environments 45, 9—20.

Smith, M., Allen, R.G., Monteith, J.L., Perrier, A., Pereira, L.S., Segeren, A., 1991. Expert Consultation on Procedures for Revision of FAO Guidelines for Prediction of Crop Water Requirements. FAO Land and Water Development Division, Rome, Italy.

Stanhill, G., 1970. Some results of helicopter measurements of albedo. Solar Energy 13, 59.

Stanhill, G., Cohen, S., 2001. Global dimming: a review of the evidence for a widespread and significant reduction in global radiation with discussion of its probable causes and possible agricultural consequences. Agricultural and Forest Meteorology 107, 255—278.

Stein, A., Staritsky, I.G., Bouma, J., Van Eijsbergen, A.C., Bregt, A.K., 1991. Simulation of moisture deficits and areal interpolation by universal cokriging. Water Resources Research 27, 1963—1973.

Stull, R.B., 1988. An Introduction to Boundary Layer Meteorology. Kluwer Academic Publishers, Dordrecht.

Sumner, D.M., Jacobs, J.M., 2005. Utility of Penman-Monteith, Priestley-Taylor, reference evapotranspiration, and pan evaporation methods to estimate pasture evapotranspiration. Journal of Hydrology 308, 81—104.

Sun, G., Zhou, G., Zhang, Z., Wei, X., McNulty, S.G., Vose, J.M., 2006. Potential water yield reduction due to forestation across China. Journal of Hydrology 328, 548—558.

Taylor, P.A., 1998. Turbulent boundary-layer flow over low and moderate slope hills. Journal of Wind Engineering and Industrial Aerodynamics, 25—47.

Thom, A.S., Thony, J.-L., Vauclin, M., 1981. On the proper employment of evaporation pans and atmometers in estimating potential transpiration. Quarterly Journal of the Royal Meteorological Society 107, 711—736.

Thornthwaite, C.W., 1948. An approach toward a rational classification of climate. The Geographical Review 38, 55—94.

Thornton, P.E., Running, S.W., White, M.A., 1997. Generating surfaces of daily meteorological variables over large regions of complex terrain. Journal of Hydrology 190, 214—251.

Ulgen, K., Hepbasli, A., 2004. Solar radiation models. Part 1: a review. Energy Sources 26, 507—520.

Varis, O., Vakkilainen, P., 2001. China's 8 challenges to water resources management in the first quarter of the 21st Century. Geomorphology 41, 93—104.

Wahba, G., 1990. Spline Models for Observational Data. Society for Industrial and Applied Mathematics, Philadelphia, Pennsylvania.

Wahba, G., Wendelberger, J., 1980. Some new mathematical methods for variational objective analysis using splines and cross validation. Monthly Weather Review 108, 1122—1143.

Wallace, J.S., 1995. Calculating evaporation: resistance to factors. Agricultural and Forest Meteorology 73, 353—366.

Wallace, J.S., 2000. Increasing agricultural water use efficiency to meet future food production. Agriculture, Ecosystems and Environment 82, 105—119.

Weber, R.O., Furger, M., 2001. Climatology of near-surface wind patterns over Switzerland. International Journal of Climatology 21, 809—827.

Wenhua, L., 2004. Degradation and restoration of forest ecosystems in China. Forest Ecology and Management 201, 33—41.

Williams, M.W., Losleben, M., Caine, N., Greenland, D., 1996. Changes in climate and hydrochemical responses in a high-elevation catchment in the Rocky Mountains, U.S.A. Limnology and Oceanography 41, 939—946.

Wilson, J.P., Gallant, J.C., 2000. Secondary topographic attributes. In: Wilson, J.P., Gallant, J.C. (Eds.), Terrain Analysis. John Wiley & Sons, Inc, New York, pp. 87—131.

Winkler, D., 2002. Participation in forestry in Tibetan Southwest China: a strategy to resolve resource use conflicts. Mountain Research and Development 22, 397—399.

Wood, N., 2000. Wind flow over complex terrain: a historical perspective and the prospect for large-eddy modelling. Boundary-Layer Meteorology 96, 11—32.

Wu, Y., Xie, K., Zhang, Q., Zhang, Y., Xie, Y., Zhang, G., Zhang, W., Ritsema, C.J., 2003. Crop characteristics and their temporal change on the Loess Plateau of China. Catena 54, 7—16.

Wu, S.H., Yin, Y.H., Zheng, D., Yang, Q.Y., 2006. Moisture conditions and climate trends in China during the period 1971-2000. International Journal of Climatology 26, 193—206.

Xiang-zhou, X., Hong-wu, Z., Ouyang, Z., 2004. Development of check-dam systems in gullies on the Loess Plateau, China. Environmental Science and Policy 7, 79—86.

Xiubin, H., Zhanbin, L., Mingde, H., Keli, T., Fengli, Z., 2003. Downscale analysis for water scarcity in response to soil-water conservation on Loess Plateau of China. Agriculture, Ecosystems and Environment 94, 355—361.

Xu, C.Y., Singh, V.P., 2002. Cross comparison of empirical equations for calculating potential evapotranspiration with data from Switzerland. Water Resources Management 16, 197—219.

Xu, Z.X., Takeuchi, K., Ishidaira, H., Zhang, X.W., 2002. Sustainability analysis for Yellow River water resources using the system dynamics approach. Water Resources Management 16, 239—261.

Xu, Z.G., Bennett, M.T., Tao, R., Xu, J.T., 2004. China's sloping land conversion programme four years on: current situation and pending issues. International Forestry Review 6, 317—326.

Xu, C., Gong, L., Jiang, T., Chen, D., Singh, V.P., 2006. Analysis of spatial distribution and temporal trend of reference evapotranspiration and pan evaporation in Changjiang (Yangtze River) catchment. Journal of Hydrology 327, 81—93.

Yang, H., 2004. Land conservation campaign in China: integrated management, local participation and food supply option. Geoforum 35, 507—518.

Yang, Q.K., Van Niel, T.G., McVicar, T.R., Hutchinson, M.F., Li, L.T., 2005. Developing a digital elevation model using ANUDEM for the Coarse Sandy Hilly Catchments of the Loess Plateau, China. CSIRO Land and Water Technical Report 7/05, Canberra, Australia, http://www.clw.csiro.au/publications/technical2005/tr7-05.

Yang, Q.K., McVicar, T.R., Van Niel, T.G., Hutchinson, M.F., Li, L.T., Zhang, X.P., in press. Improving a digital elevation model by reducing source data errors and optimising interpolation algorithm parameters: an example in the Loess Plateau, China. International Journal of Applied Earth Observation and Geoinformation. doi:10.1016/j.jag.2006.08.004.

Ye, Y.Q., Chen, G.J., Fan, H., 2003. Impacts of the ''Grain for Green'' project on rural communities in the Upper Min River basin, Sichuan, China. Mountain Research and Development 23, 345—352.

Yoshino, M.M., 1975. Climate in a Small Area: An Introduction to Local Meteorology. University of Tokyo Press, Tokyo.

Zhai, P., Sun, A., Ren, F., Liu, X., Gao, B., Zhang, Q., 1999. Changes of climate extremes in China. Climatic Change 42, 203—218.

Zhang, J., Lin, B., 1992. Climate of China. John Wiley & Sons, New York.

Zhang, L., Dawes, W.R., Walker, G.R., 2001. Response of mean annual evapotranspiration to vegetation changes at catchment scale. Water Resources Research 37, 701—708.

Zhang, X.P., Zhang, L., McVicar, T.R., Van Niel, T.G., Li, L.T., Li R., Yang, Q.K., Liang, W., in press. Modeling the impact of afforestation on mean annual streamflow in the Loess Plateau, China. Hydrological Processes.

Zhu, T.X., Band, L.E., Vertessy, R.A., 1999. Continuous modeling of intermittent stormflows on a semi-arid agricultural catchment. Journal of Hydrology 226, 11—29.